Use of 3D mathematical modelling to understand the heat transfer mechanisms during freeze-drying using high-throughput vials

Juan Patricio Buceta, Stephanie Passot, Bernadette Scutellà, Erwan Bourlés, Fernanda Fonseca, Ioan-Cristian Trelea

Use of 3D mathematical modelling to understand the heat transfer mechanisms during freeze-drying using high-throughput vials

Juan Patricio Buceta[1], Stéphanie Passot[1], Bernadette Scutellà[2], Erwan Bourlés[2], Fernanda Fonseca[1], Ioan CristianTrelea[1]

[1] Université Paris-Saclay, INRAE, AgroParisTech, UMR SayFood, F-78850, Thiverval-Grignon, France

[2] GSK, Rixensart, Belgium

1. Abstract

Screening potential vaccine formulations during freeze-drying is a time-consuming task. High-throughput systems, consisting of small vials inside aluminium well plates, can accelerate formulation selection. However, heat transfer variations among vials due to the edge effect can entail deviations in the final product quality and bias results. This work investigates how the vial position in the well plate impacts the heat flow received during the primary drying step of freeze-drying. Two 3D steady-state models were proposed and compared to evaluate the effect of time passing. One model, called the *distilled water model*, represents vials containing only a frozen layer at the beginning of primary drying. A second model, called the *product model*, represents vials containing frozen and dried product layers after drying has progressed (up to half of the product dried). Heat transfer models were validated using heat flows determined by gravimetric analysis during sublimation tests (shelf temperatures -40 and -15 °C, chamber pressures from 4 to 65 Pa). At the beginning of primary drying, the *distilled water model* indicated that vials facing a chamber wall received heat flows up to 25% greater than those in the centre of the well plate. As sublimation progressed (*product model*), the dried product layer resistance to mass transfer tended to counterbalance the impact of the chamber wall.

Keywords: Lyophilisation; vaccines; 3D modelling; well plate; edge effect; vial heat transfer coefficient; inter-vial heterogeneity; product resistance.

2. **Abbreviations**

Latin alphabet

A	Transfer area	m^2
d_{gas}	Molecular diameter of the water molecule	m
d_C	Distance between the shelves and the chamber surface	m
d_E	Distance between the edge of the bottom shelf and the well plate	m
d_{VE}	Outer diameter of the vial	m
d_{VI}	Inner diameter of the vial	m
d_S	Separation between shelves	m
F	Visualisation factor	Dimensionless
G	Irradiation	$W.m^{-2}$
h_{well}	Depth of the wells	m
J	Radiosity	$W.m^{-2}$
K	Heat transfer coefficient	$W.m^{-2}.K^{-1}$
k	Boltzmann constant	$J.K^{-1}$
l	Layer thickness	m
l_d	Dried product layer thickness	m
l_{fp}	Mean free path	m
m_f	Mass of the vial after ice sublimation experiments	Kg
m_i	Mass of the vial before ice sublimation experiments	Kg
P_C	Pressure inside the chamber	Pa
P_{sat}	Ice-vapour equilibrium pressure	Pa
P_t	Water triple point pressure	Pa
q	Heat flux	$W.m^{-2}$
$\dot{Q}$	Heat flow rate received by a vial	W
$\dot{Q}_{exp}$	Experimental heat flow rate	W
R	Ideal gas constant	$J.K^{-1}.mol^{-1}$
R_P	Area-normalised dried product resistance	$Pa.s.m^2.kg^{-1}$
T	Temperature	K
T_{sat}	Ice-vapour equilibrium temperature	K
T_{shelf}	Shelf temperature	K
T_t	Water triple point temperature	K
T_{vial}	Vial surface temperature	K
T_{wall}	Chamber wall surface temperature	K
T_{WP}	Well plate surface temperature	K
V_i	Ice volume	m^3
V_p	Product volume (sum of dried and frozen product volumes)	m^3

Greek alphabet

α	Thermal accommodation coefficient for the gas conduction	Dimensionless
ΔH_{sub}	Mass latent heat of sublimation	J.kg^{-1}
$\widetilde{\Delta H_{sub}}$	Molar latent heat of sublimation	J.mol^{-1}
Δt	Duration of the ice sublimation experiment	s
ε_{dry}	Emissivity of the dried product layer	Dimensionless
ε_{ice}	Emissivity of the ice	Dimensionless
ε_{shelf}	Emissivity of the shelf	Dimensionless
ε_{vial}	Emissivity of the vial	Dimensionless
ε_{wall}	Emissivity of the chamber wall	Dimensionless
ε_{wp}	Emissivity of the well plate	Dimensionless
λ	Thermal conductivity	W.m^{-1}.K^{-1}
λ_{dry}	Thermal conductivity of the dried product layer	W.m^{-1}.K^{-1}
λ_{gas}^{cont}	Gas thermal conductivity in continuous regime	W.m^{-1}.K^{-1}
λ_{gas}^{fm}	Gas thermal conductivity in free molecular regime	W.m^{-1}.K^{-1}
λ_{ice}	Thermal conductivity of the ice	W.m^{-1}.K^{-1}
Λ_0	Free molecular heat conductivity of the gas at 0 °C	W.m^{-2}.K^{-1}.Pa^{-1}
σ	Stefan-Boltzmann constant	W.m^{-2}.K^{-4}
ϱ	Surface reflectivity	Dimensionless

Superscript

B	Referring to the heat transfer between the well and the vial bottom
c	Conduction within a body
cc	Contact conduction between solids
gc	Gas conduction contribution
rad	Radiation contribution
S	Referring to the heat transfer between the well and the vial lateral side

Subscript

HV	Referring to the heat transfer from the well plate to the high-throughput vial
WP	Referring to the heat transfer from the shelf to the well plate
1	Referring to surface 1
2	Referring to surface 2
$1 \rightarrow 2$	From surface 1 to surface 2

3. Introduction

Freeze-drying or lyophilisation is a drying process that consists of three stages: (i) freezing the product solution, (ii) removing the frozen solvent (usually water) by sublimation (primary drying), and (iii) removing the unfrozen solvent by desorption (secondary drying). The low temperatures reached by the product make freeze-drying suitable to preserve thermolabile products like vaccines and proteins, among others [1–3].

The increasing demand for new vaccines pushes researchers to accelerate the development stage of formulations. The use of high- throughput vials systems consisting of aluminium 96-well plates and small tubular vials (maximal volume 1000 µL [4,5]) can improve the time efficiency during formulation screening for product development. High-throughput vial systems permit the placement of over twice the amount of containers on the shelf than serum vials (traditional container) [5,6] while also requiring fewer quantities of the active ingredient for the same number of tested formulations. Changing the container during the formulation development step implies modifications in the heat and mass transfer properties compared to the primary packaging used at the production scale (serum vials) [6,7]. A graphical solution has been recently developed to manage the process scale-up and scale-down between both types of product containers (high-throughput vials used for formulation development and serum vials for production) [5]. This previous work showed that the heat transfer coefficients between the shelf and the vial bottoms (commonly denoted as K_V) were almost three times greater in high throughput vials than in serum vials in the usual range of conditions used in pharmaceutical freeze-drying [5].

The product temperature is a critical quality parameter [8–10] and should remain lower than a specific value during primary drying – known as collapse temperature – to preserve the product structure obtained by freezing and attain an acceptable final product appearance [11]. Moreover, obtaining a freeze-dried product with a low moisture content (generally below 3%), a rapid reconstitution time, and no potency reduction, depends greatly on avoiding product collapse during primary drying. Several factors can affect the heat and mass transfer balance and the resulting product temperature; for example, the operating conditions (i.e. shelf temperature and chamber pressure) [12,13], the geometry of the containers (usually vials), [6,14], and their location on the shelf [15,16].

Previous experimental data suggest that the heat flow contribution from the chamber walls may not be negligible for serum vials located at the edge of the vials' arrangement on the shelf [e.g. 7,15,18–20,24].

Many authors represented these “extra” heat flow contributions as a higher value of the heat transfer coefficient between the shelf and the vial (K_V) for vials at the edge compared to those in the centre [e.g. 7,15,18–20,24], and estimated the product temperature using lumped-parameter models (0D models) for different vial positions [22,23], with the assumption that shelves are the only heat sources in the system [24]. However, the theoretical groud behind the modification of K_V to account for the heat transfer from these extra sources (e.g. chamber walls and door) may be questioned since their temperatures are different from those of the shelves (K_V was defined for the temperature difference between the vials and the shelf). Recently, a 3D steady-state model of the heat transfer during the sublimation step highlighted conduction through low-pressure water vapour as the dominant heat transfer mechanism to serum vials, also explaining the extra heat transfer to serum vials at the edge compared to central ones [21]. 3D modelling serves thus to avoid the shortcut of using K_V, detailing heat transfer mechanisms for each heat source (e.g. shelves, chamber walls) and their relative importance. However, the previous 3D model [21] did not consider the resistance to mass transfer through the dried product layer when a pharmaceutical formulation was processed. Therefore, such a 3D model could not predict how the heat flow rate variation between vial positions would evolve throughout primary drying.

A similar edge effect is expected between high-throughput vials in a well plate, where high-throughput vials near a well plate edge may receive greater heat flows than those in the centre (surrounded by other vials). However, no research has been carried out on this matter to the best of our knowledge.

The main novelty of this paper was the extension of the 3D model previously developed for serum vials [21] to represent the heat transfer mechanisms between the well plate and the high-throughput vials, as well as to include the mass transfer through the dried product layer and its coupling to the heat transfer. The present work thus aimed at better understanding the contribution of individual heat transfer mechanisms in high-throughput systems, the edge effect, and the impact of the product resistance associated with the progress of primary drying. We have considered primary drying as a succession of heat and mass transfer equilibria [12,18], and studied the time effect using steady-state models representing different positions of the sublimation front. Based on the work of Scutellà et al. [21], two 3D steady-state models for heat and mass transfer during primary drying in high-throughput vials were thus proposed to consider the progress of time: (i) the *distilled water model*, and (ii) the *product model*. The *distilled water model* represented the beginning of primary drying when there is no dried product in the vials (only ice). The *product model* represented two stages during primary drying with two different

thicknesses of a dried product layer (0.1 and 5 mm). Finally, a sensitivity analysis was performed with the *product model*, which indicated the parameters that should be measured carefully for a better estimation of the heat flows received by the vials.

4. **Experimental data**

4.1. Materials

Ice sublimation experiments were performed using the *96-Well Freeze-Drying System* manufactured by VirTis (SP Scientific, Stone Ridge, New York, USA), comprising aluminium well plates with a black matte finish and tubular glass vials (non-siliconised), as shown in Figure 1a. Two vial sizes were employed, both presenting the same diameter but differing in height, and consequently, in the maximal filled volume: (i) 500-µL (Figure 1a, left), and (ii) 1000-µL (Figure 1a, right). Figure 1b presents a picture of the vials and well plates inside a freeze dryer. Experiments were performed in an Epsilon 2-25D pilot scale freeze dryer (Martin Christ Gefriertrocknungsanlagen GmbH, Osterode am Harz, Germany). The freeze dryer had a drying chamber with a total volume of 0.38 m^3, and a capacitive manometer monitored the chamber pressure. Inside the chamber, there were seven shelves of 0.27 m^2 each; the distance between shelves was 57 mm.

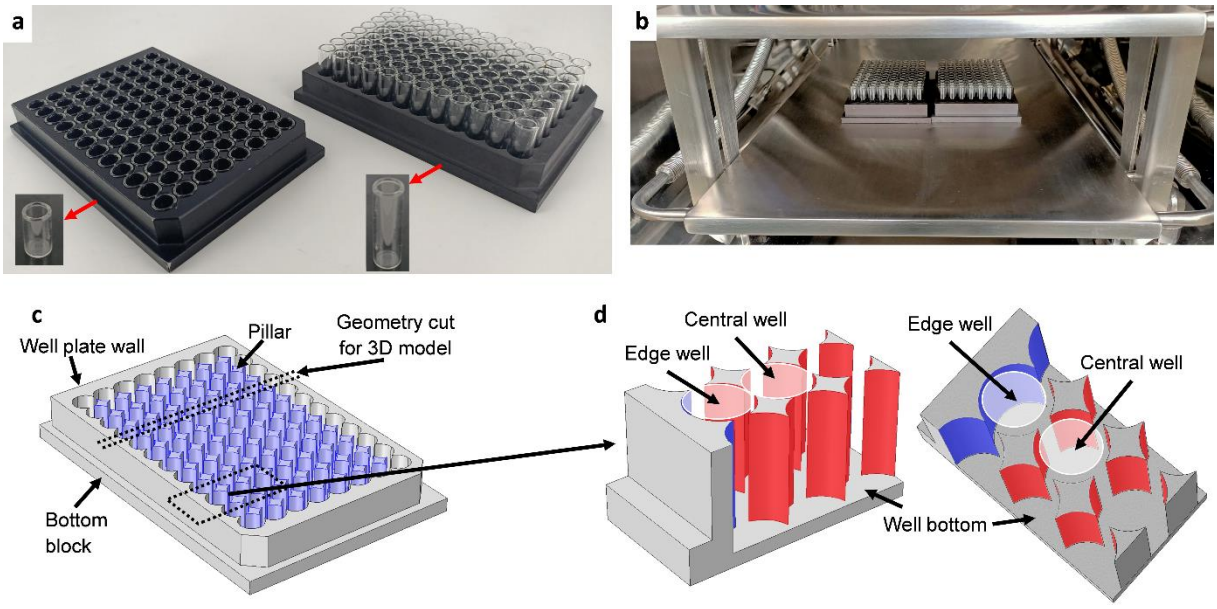

Figure 1 – Vials and well plate geometry. (a) Well plates filled with 500-µL vials (left) and 1000-µL vials (right). (b) Well plates and vials inside a freeze-dryer. (c) Well plate geometry with pillars coloured purple. (d) Geometry details with different view angles. Red surfaces are the pillar surfaces facing the vial. Blue surfaces are the well plate wall surfaces facing the vial.

4.2. Methods

Experimental heat flow rates received by vials were measured through gravimetric analysis, as detailed in Buceta et al. [5]. 500-µL vials were filled with 400 µL of distilled water, and 1000-µL vials were filled with 600 µL of distilled water. No stoppers were placed on the vial necks. Tempris wireless temperature probes (iQ-mobil solution GmbH, Holzkirchen, Germany) were used to register the ice temperature in six 1000-µL vials. Two well plates containing vials of the same size were loaded on the centre of the shelf pre-cooled at -50 °C. The freezing step lasted for 2 hours, then the sublimation step started by decreasing the pressure inside the chamber and increasing the shelf temperature at 1 °C.min^{-1} up to the set point. The inlet temperature of the heat-transfer fluid circulating inside the shelves was set to either -40 or -15 °C during sublimation. Furthermore, the shelf temperature was considered equal to the average between the inlet and the outlet temperature of the heat-transfer fluid due to the great conductivity of the metallic shelves. At a shelf temperature of -40 °C, the chamber pressure was set to 4 Pa, and at -15 °C, the chamber pressures tested were 4, 6, 12, 25, and 65 Pa. The sublimation step lasted until approximately 20% of each vial's initial ice content was removed, then this step was ended by rapidly breaking the vacuum inside the drying chamber. Vials were weighed before and after ice sublimation experiments using a robotic tube handler model XL9 manufactured by BioMicroLab (Concord, California, USA) with an analytical scale (± 1×10^{-7} kg). Time-averaged heat flows throughout the experiment ($\dot{Q}_{exp}$) were calculated for each vial as [6,7]:

$$\dot{Q}_{exp} = \frac{m_i - m_f}{\Delta t} \Delta H_{sub} \quad (1)$$

The significance of all symbols is given in the Nomenclature. The sublimation was considered to start when the shelf temperature was higher than the ice-vapour equilibrium temperature at the chamber pressure, and finish when the vacuum was broken.

The temperature of the chamber walls was measured using Tempris wireless temperature probes (iQ-mobil solution GmbH, Holzkirchen, Germany) fixed using heat conductive tape during ice sublimation experiments at a chamber pressure of 4 Pa and a shelf temperature of -40 and -15 °C.

5. Heat and mass transfer model

5.1. Well plate geometry

High-throughput vials were positioned inside aluminium well plates to keep them in place during freeze-drying, as shown in Figure 1a and 1b. Figure 1c presents a 3D reconstruction of a well plate, indicating the main components: (i) the bottom block, (ii) the well plate wall, and (iii) the pillars. The geometry is not the same for all wells of the well plate; two types of well positions were distinguished: (i) well positions next to a well plate wall hereinafter referred to as edge wells (Figure 1d); (ii) well positions non-contiguous to a well plate wall hereinafter referred to as central wells (Figure 1d). Edge wells have four surfaces facing the vials: a bottom surface (Figure 1d), two lateral surfaces belonging to the two metallic pillars around (Figure 1d, red surfaces), and one lateral surface belonging to the well plate wall (Figure 1d, blue surface). Central wells have five surfaces facing the vials: a well bottom surface (Figure 1d), and four lateral surfaces belonging to the four metallic pillars around (Figure 1d, red surfaces).

Due to the dimensions and geometry of the system, it is not possible for the vials to touch either four pillars (in the case of central vials) or two pillars and the well plate wall (in the case of edge vials) simultaneously. Therefore, for all vials and well positions, physical contact was only considered between: (i) the vial side and only two pillars referred to as “physical contact” pillars, and (ii) the vial bottom and the well bottom. Note that the differences between edge and central wells did not imply that edge wells and vials had more physical contact than central wells and vials; thus, all well and vial positions were assumed to have the same physical contact.

5.2. Model geometry

3D models represented ice sublimation using 500-µL or 1000-µL vials inside the well plate filled with either distilled water or a “model” product (5% w/w sucrose aqueous solution). Figure 2a shows the geometry used for 500-µL vials as an example, the geometry for 1000µL vials is similar (with higher vial and content heights). Each geometry represented: (i) a portion of the drying chamber wall, (ii) a fragment of the top and bottom shelves; (iii) eight half-vials (two edge half-vials and six central half-vials), all filled with either an ice layer or presenting a dried product layer and a frozen product layer (Figure 2b); (iv) the section of the well plate where the vials were placed, including four physical contact pillars (red arrow in Figure2a) and three non-physical contact pillars, so each half-vial “rested” on one physical contact pillar.

Edge vials and edge wells in the geometry were further subdivided according to the well plate position on the shelf (Figure 2a): (i) edge positions facing a chamber wall were referred to as outer edge positions, and (ii) edge positions facing another well plate were referred to as inner edge positions.

Different 3D geometries were built depending on the vial size and content. The model considering all vials filled with an ice layer (only) is referred to as the *distilled water model*, and the model considering all vials presenting a dried product layer and a frozen product layer is referred to as the *product model*. In the *distilled water model*, the vial content was only an ice cylinder [21] with a volume equal to 90% of the initial ice volume used in the sublimation experiments. This represents an “average” situation during the laboratory experiments between the beginning of the ice sublimation (0% of the ice mass was removed) and the end (approximately 20% of the ice mass removed). In the *product model*, the vial content was a cylinder of frozen product with a cylinder of dried product on top; the total volume of both cylinders was considered equal to the initial ice volume used in the sublimation experiments. All dimensions relevant to the 3D model geometry are reported in Table 1.

When considering the dynamics of the primary drying step, the *distilled water model* can be associated with the beginning of this step, where the dried layer is not yet present. In contrast, the *product model* represents an intermediate moment during primary drying, after the appearance and progress of a sublimation front (ice-vapour interface) that moves from the top to the bottom of the vial content, leaving a dried product layer above the remaining frozen product layer (Figure 2b).

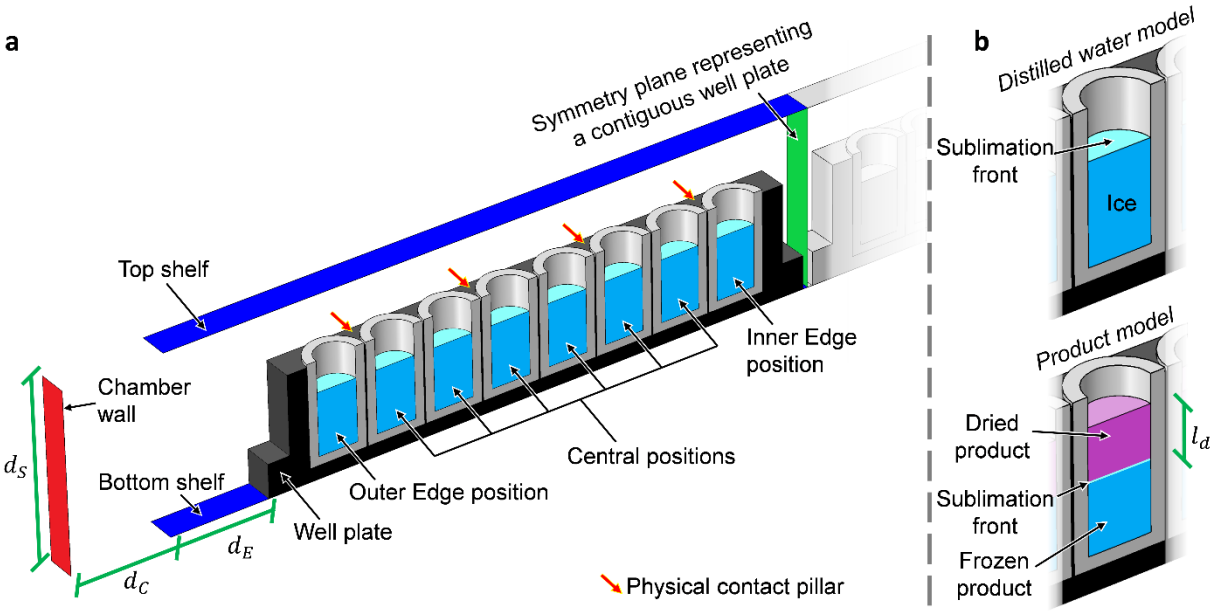

Figure 2 – Model geometry (not in scale) for 500-µL vials in well plates. (a) Overall view, with only the vials closer to the chamber wall represented for clarity. (b) Detail of the vial and its content for distilled water and product models. d_S is the vertical distance separating shelves, d_C is the distance between the shelf and the chamber wall, d_E is the distance between the edge of the shelf and the well plate, and l_d is the dried product layer thickness.

Table 1 – Relevant physical constants, geometric dimensions, and other model parameters from the literature.

Parameter	Value	Units	Source
Physical constants			
d_{gas}	2.8×10^{-10}	m	[26]
k	1.38×10^{-23}	$J.K^{-1}$	[27]
P_t	612	Pa	[27]
R	8.3144	$J.K^{-1}.mol^{-1}$	[27]
T_t	273.16	K	[27]
α	0.87	Dimensionless	[24]
ΔH_{sub}	2.763×10^{6}	$J.kg^{-1}$	[6]
$\widetilde{\Delta H_{sub}}$	5.11×10^{4}	$J.mol^{-1}$	[28]
ε_{dry}	0.95	Dimensionless	[29]
ε_{ice}	0.98	Dimensionless	[30]
ε_{shelf}	0.18	Dimensionless	[5]
ε_{vial}	0.85	Dimensionless	[5]
ε_{wall}	0.13	Dimensionless	[5]
ε_{wp}	0.87	Dimensionless	[5]
Λ_0	1.99	$W.m^{-2}.K^{-1}.Pa^{-1}$	[24]
σ	5.67×10^{-8}	$W.m^{-2}.K^{-4}$	[27]
λ_{gas}^{cont}	0.025	$W.m^{-1}.K^{-1}$	[31]
λ_{ice}	2.23	$W.m^{-1}.K^{-1}$	[32]
λ_{dry}	0.043	$W.m^{-1}.K^{-1}$	5% of the sucrose thermal conductivity [33,34]
Geometric dimensions			
d_C	1.08×10^{-1}	m	Measured
d_E	1.40×10^{-1}	m	Measured
d_S	5.7×10^{-2}	m	Measured
d_{VE}	8.82×10^{-3}	m	[5]
d_{VI}	7.20×10^{-3}	m	[5]
h_{well}	1.525×10^{-2}	m	[5]
l_d	1×10^{-4} or 5×10^{-3}	m	Consideration for this work
l_{HV}^{B}	6.7×10^{-5}	m	[5]
l_{HV}^{S}	2.3×10^{-4}	m	[5]
V_i	392	µL	90% of the initial ice volume
	589		
V_p	436	µL	Initial frozen volume

	654		
Other model parameters			
l_{fp}	1.0×10^{-3}	m	Calculated using Equation (5)
R_P	0.119×10^{5}	Pa.s.m^2.kg^{-1}	[35]
	1.248×10^{5}		
T_{wall}	0.1	°C	Measured
	5.1		

5.3. Distilled water model

The *distilled water model* was developed and validated based on the laboratory ice sublimation experiments described in Section 4.2. The heat transfer mechanisms considered in this work are schematised in Figure 3. Figure 3a and 3b refer to the heat transfers between surfaces and within bodies at a macroscopic scale, while Figure 3c represents the heat transfers between surfaces at a microscopic scale. The heat transfer mechanisms of the model were:

(i) *Conduction through solids*, concerning the well plate, vials, and ice (yellow arrows in Figure 3a and 3b).

(ii) *Contact conduction between solids*, including the contact between the bottom shelf and the well plate bottom, the wells (bottom and physical contact pillars) and the vials (red triangles in Figure 3c), and the vials and the ice (red dashes in Figure 3c).

(iii) *Conduction through the gas* (green arrows in Figure 3a and 3c); the thermal conductivity of gases in vacuum conditions depends on the gas regime, according to the ratio between the average distance a gas molecule travels between collisions with other molecules (mean free path) and the separation between surfaces.

(iv) *Radiation* emitted and received by the wall, both shelves, the well plate, the vials, and the ice (orange "lightning" arrows in Figure 3a and 3c).

Heat transfer by convection was considered negligible, as previously proved by other authors in similar operating conditions [16,25,36]. To support this assumption, the Rayleigh number (Ra) near the vials was estimated to be between 300 and 1300 depending on the operating conditions, which is lower than the critical value required for a significant contribution of heat transfer by convection ($Ra > 1700$; [27,37]).

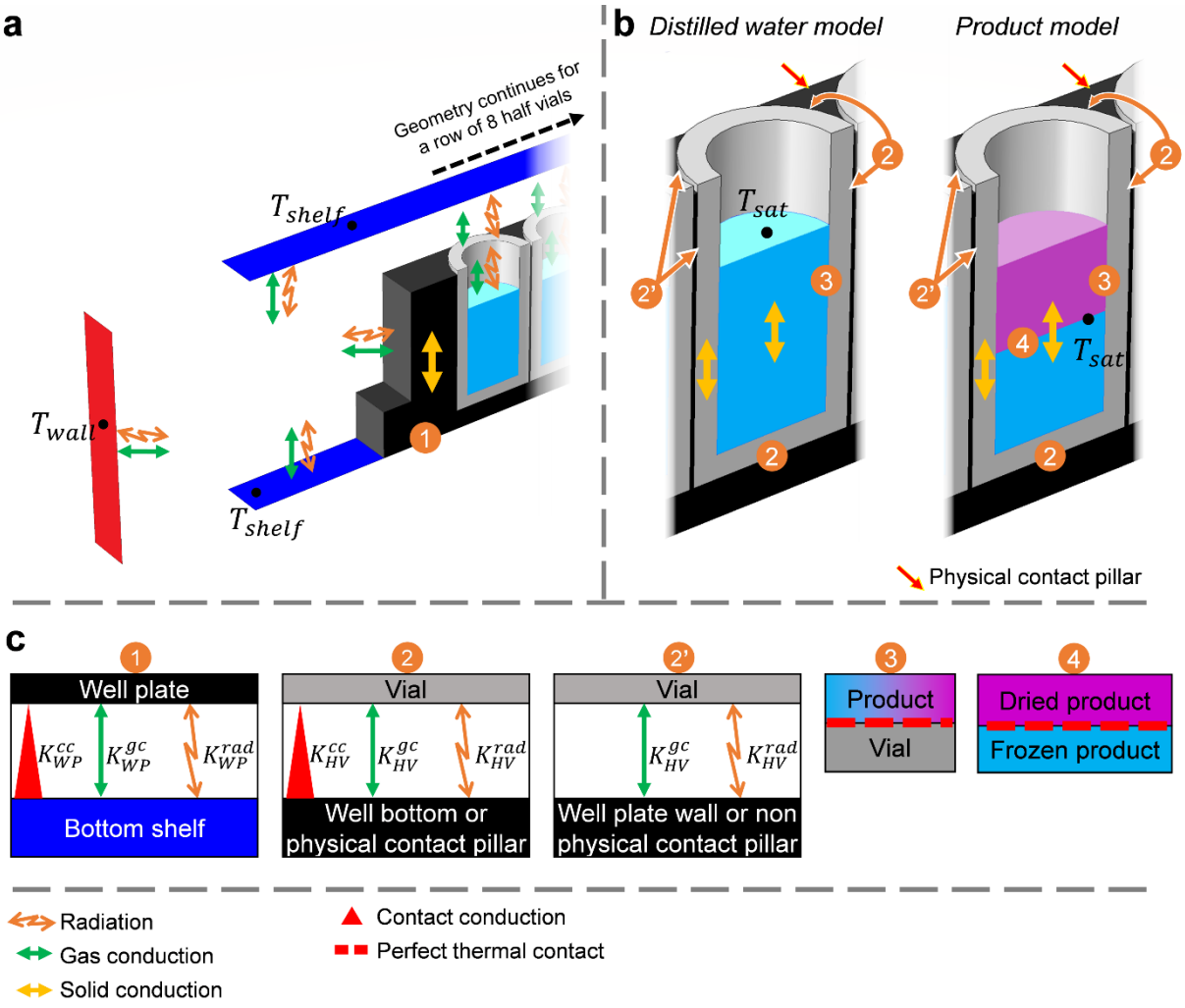

Figure 3 – Schematic representation (not in scale) of the main heat transfer mechanisms and fixed temperatures in the analysed system. (a) Overall view, only the vials closer to the chamber wall are represented for clarity. (b) Details of the mechanisms within the vial and its content for the distilled water and product models. (c) Heat transfer mechanisms at a microscopic scale. K_{WP} *and* K_{HV} *are detailed according to the individual heat transfer mechanism involved:* K^{cc} *by contact conduction,* K^{gc} *by conduction through the gas trapped between the surfaces,* K^{rad} *by radiation.*

5.3.1.Conduction through solids

At a microscopic scale, thermal conduction within a body is the mechanism by which heat is transferred due to collisions between the body particles [27]. At a macroscopic scale, the conductive heat flux (q^c) within the solids (well plate, vials, and ice) were calculated using Fourier's law:

$$q^c = \lambda \nabla T \tag{2}$$

Conductivity values are reported in Table 1.

5.3.2.Contact conduction between solids

Heat transfer by contact conduction occurs between solids directly touching each other and depends on the macroscopic (apparent) contact area and the microscopic state of the surface, such as roughness. The contact conduction heat flux between the bottom shelf and the well plate bottom (q_{WP}^{cc}), symbolised by a red triangle in Figure 3c, was calculated as:

$$q_{WP}^{cc} = K_{WP}^{cc}\left(T_{shelf} - T_{WP}\right) \tag{3}$$

Similarly, the contact conduction heat flux (q_{HV}^{cc}) between the well bottoms and the vial bottoms, and between the physical contact pillars and the vial sides, symbolised by red triangles in Figure 3c, were calculated as:

$$q_{HV}^{cc} = K_{HV}^{cc}(T_{WP} - T_{vial}) \tag{4}$$

K_{WP}^{cc} and K_{HV}^{cc} were estimated based on experimental data as detailed in Section 6.4, and values are reported in Table 2. The heat transfer mechanism between the vials and the ice, symbolised by a red dashed line in the orange dot 3 of Figure 3c, was considered perfect contact conduction (zero resistance to the heat transfer). Hence, the local temperature of the vial and the ice was the same at their contact surface.

Table 2 – Values of parameters estimated based on measured heat flow data for 500-µL vials at a shelf temperature of -15 °C and chamber pressures of 4, 12, and 65 Pa.

Parameter	Mean value in this work	95 % Confidence interval		Units
		This work	[5]*	
Heat transfer from the bottom shelf to the well plate bottom				
K_{WP}^{cc}	5.1	1.6 – 8.6	2.4 – 4.8	$W.m^{-2}.K^{-1}$
α_{WP}	0.95	0.60 – 1.00**	0.76 – 0.93	Dimensionless
l_{WP}	4.20×10^{-4}	2.46×10^{-4} – 5.29×10^{-4}	2.23×10^{-4} – 2.58×10^{-4}	m
Heat transfer from the wells to the vials				
K_{HV}^{cc}	20.1	12.1 – 28.1	59.7 – 66.5	$W.m^{-2}.K^{-1}$
α_{HV}	0.33	0.29 – 0.37	0.18 – 0.32	Dimensionless

** Values reported for 500-µL vials in a "B-type well plate", which refers to a well plate type described in Buceta et al.* [5].

*** Upper bound truncated to the maximum possible physical value.*

5.3.3.Conduction through the gas

The heat transfer by conduction through the gas phase in the system was divided as: (i) gas conduction within the chamber, concerning the largest gas volume in the chamber, symbolised by green arrows in Figure 3a; or (ii) conduction through the gas trapped between adjacent surfaces (i.e. between the bottom shelf and the well plate bottom, and between the wells and the vials), symbolised by green arrows in Figure 3c.

5.3.3.1. Gas conduction within the chamber

All the gas in the freeze dryer chamber was assumed to be water vapour [24]. Heat transfer by conduction through the gas within the chamber (Figure 3a) was considered under a continuous regime with a boundary layer of free molecular regime next to all the solids in the chamber (i.e. wall, shelves, well plate, vials, and ice; Figure 3a). Scutellà et al. [21] fixed the boundary layer thickness as a value relatively small compared to the serum vial geometry. Similarly, in our work, the boundary layer thickness was selected as the mean free path (l_{fp} = 1 mm) calculated at 10 Pa (usual chamber pressure value used in pharmaceutical freeze-drying) and -15 °C (= 258.15 K, usual shelf temperature value) as [38]:

$$l_{fp} = \frac{k \times 258.15\ [K]}{\sqrt{2}\pi {d_{gas}}^2 \times 10\ [Pa]} \quad (5)$$

The effective diameter of the water molecule (d_{gas}) is given in Table 1. Fourier's law (Equation (2)) was used to model the conductive heat flux within the gas, and the thermal conductivity depended on the gas regime. Outside of the boundary layer (gas portion farther than a mean free path from the solids), the gas was considered under a continuous regime and the thermal conductivity (λ_{gas}^{cont}) was that of water vapour at atmospheric pressure [21]. Inside the boundary layer (gas portion closer than a mean free path from the solids), the gas was considered under a free molecular regime, and the thermal conductivity (λ_{gas}^{fm}) was calculated as [21]:

$$\lambda_{gas}^{fm} = \alpha \Lambda_0 P_C l_{fp} \quad (6)$$

Relevant constant values are reported in Table 1.

5.3.3.2. Conduction through the gas trapped between adjacent surfaces

The heat flux by conduction through the trapped gas between the bottom shelf and the well plate bottom (q_{WP}^{gc}), symbolised by a green arrow in the orange dot 1 of Figure 3c, was expressed as:

$$q_{WP}^{gc} = K_{WP}^{gc}\left(T_{shelf} - T_{WP}\right) \quad (7)$$

Similarly, the heat flux by conduction through the trapped gas between the wells and the vials (q_{HV}^{gc}), symbolised by a green arrow in Figure 3c, was given by:

$$q_{HV}^{gc} = K_{HV}^{gc}(T_{WP} - T_{vial}) \quad (8)$$

The heat transfer by conduction through gas trapped between adjacent surfaces is traditionally assumed under a transition regime between free molecular and continuous regimes [6,7,24,39]. K_{WP}^{gc} was thus calculated as [24]:

$$K_{WP}^{gc} = \frac{\alpha_{WP}\Lambda_o P_C}{1 + \frac{l_{WP}}{\lambda_{gas}^{cont}}\alpha_{WP}\Lambda_o P_C} \quad (9)$$

Likewise, K_{HV}^{gc} was calculated as:

$$K_{HV}^{gc} = \frac{\alpha_{HV}\Lambda_o P_C}{1 + \frac{l_{HV}}{\lambda_{gas}^{cont}}\alpha_{HV}\Lambda_o P_C} \quad (10)$$

The average distance between the well and the vial vial bottom (l_{HV}^{B}) was considered as the average vial bottom concavity, and l_{HV} between the well's pillars and the vial sides (l_{HV}^{S}) was considered as the difference between the well radius and the outer radius of the vial. Parameters α_{WP}, α_{HV}, and l_{WP} were estimated using experimental data, and values are reported in Table 2. The parameter values and physical constants taken from the literature are gathered in Table 1.

5.3.4.Radiation

Heat transfer by radiation refers to the transmission of heat as waves through a transparent or translucent medium (in this case, the gas phase). Solid surfaces of the chamber wall, shelves, well plate, vials, and ice were considered diffuse grey-bodies with constant emissivity values (ε). The gas was modelled as transparent to radiation (ε = 0).

The heat transfer by radiation was divided as: (i) radiation between distant surfaces, concerning all surfaces of the geometry in contact with the gas within the chamber, symbolised by orange "lightning" arrows in Figure 3a; or (ii) radiation between adjacent surfaces (i.e. between the bottom shelf and the

well plate bottom, and between the wells and the vials), symbolised by orange “lightning” arrows in Figure 3c.

5.3.4.1. Radiation between distant surfaces

In the case of radiation between distant surfaces (Figure 3a), the heat flow transmitted by radiation from a surface 1 to a surface 2 ($Q_{1\to2}^{rad}$) was calculated as [40]:

$$Q_{1\to2}^{rad} = A_1 F_{1\to2}(J_1 - J_2) \tag{11}$$

The radiative heat flux of each surface was calculated as:

$$J = \varrho G + \varepsilon\sigma T^4 \tag{12}$$

In this way, the irradiation received by each surface (G) depends on the radiative heat fluxes (J) of the other surfaces and the system's geometry.

5.3.4.2. Radiation between adjacent surfaces

The heat flux by radiation between the bottom shelf and the well plate bottom (q_{WP}^{rad}), symbolised by orange “lightning” arrows in Figure 3c, was calculated using the Stefan-Boltzmann’s law for two parallel diffuse grey-body surfaces of equal areas [6]:

$$q_{WP}^{rad} = K_{WP}^{rad}\left(T_{shelf} - T_{WP}\right) \tag{13}$$

The heat transfer coefficient by radiation between the bottom shelf and the well plate bottom (K_{WP}^{rad}) was calculated as [27]:

$$K_{WP}^{rad} = \sigma \frac{1}{\frac{1-\varepsilon_{shelf}}{\varepsilon_{shelf}} + \frac{1-\varepsilon_{WP}}{\varepsilon_{WP}} + 1}\left(T_{shelf} + T_{WP}\right)\left(T_{shelf}^2 + T_{WP}^2\right) \tag{14}$$

Likewise, the radiation flux between the wells and the vials (q_{HV}^{rad}), symbolised by orange arrows in orange dots 2 and 2’ of Figure 3c, was calculated according to Stefan-Boltzmann’s law as:

$$q_{HV}^{rad} = K_{HV}^{rad}(T_{WP} - T_{vial}) \tag{15}$$

The heat transfer coefficient by radiation between the wells and the vials (K_{HV}^{rad}) was calculated as:

$$K_{HV}^{rad} = \sigma \frac{1}{\frac{1-\varepsilon_{WP}}{\varepsilon_{WP}} + \frac{1-\varepsilon_{vial}}{\varepsilon_{vial}} + 1}(T_{WP} + T_{vial})(T_{WP}^2 + T_{vial}^2) \tag{16}$$

Constant values are given in Table 1.

.

5.3.5. Ice-vapour equilibrium

The temperature at the sublimation front (T_{sat}) was set as the ice-vapour equilibrium temperature calculated using the Clausius Clapeyron relation [27]:

$$T_{sat} = \frac{T_t}{1 - \frac{RT_t}{\widetilde{\Delta H_{sub}}} ln\left(\frac{P_{sat}}{P_t}\right)} \quad (17)$$

For the *distilled water model*, P_{sat} was assumed equal to P_C based on the hypothesis that the chamber is saturated with water vapour and neglecting the vapour pressure loss between the sublimation front and the chamber.

5.4. Product model

When considering partially dried product inside the vials (as opposed to vials filled with only ice), a porous dried product layer builds up above the ice sublimation interface (Figure 2b and Figure 3). The heat and mass transfer model with a "model" product (5% sucrose aqueous solution), referred to as the *product model*, was developed by extending the *distilled water model* presented in Section 5.3.

5.4.1. Heat transfer

The heat transfer equations of the *product model* were the same as for the *distilled water model* apart from the following modifications.

(i) *Conduction through solids:* heat transfer inside the dried product layer was also considered and represented using Equation (2).

(ii) *Conduction between solids:* the heat transfer mechanism between the frozen layer and the dried product layer (Figure 3c, orange dot 4) was considered to be perfect contact conduction (zero resistance to the heat transfer) since the product forms a continuous body, so the local temperature of the frozen and dried product layers was the same (equal to T_{sat}) at their junction.

(iii) *Conduction through the gas within the chamber* and *radiation between distant surfaces* concerned the top dried product layer surface (instead of the top ice surface considered in the *distilled water model*). The physical properties of the frozen product were considered the same as ice [6]. The emissivity value of the dried product (ε_{dry}) was considered as 0.95 [29]. Moreover, the thermal conductivity of the dried product (λ_{dry}) used in Equation (2) was defined, according to Smith et al. [33], as the thermal conductivity of sucrose (0.85 $W.m^{-1}.K^{-1}$ for a 50% aqueous sucrose gel [34]) multiplied by the sucrose mass fraction of the initial solution (0.85 $W.m^{-1}.K^{-1}$ × 5% = 0.043 $W.m^{-1}.K^{-1}$).

5.4.2.Mass transfer

Mass transfer is involved in the heat transfer calculation through the ice-vapour equilibrium temperature (T_{sat}). T_{sat} was calculated with Equation (17), but the pressure at the sublimation front (P_{sat}) was modified considering the vapour pressure loss within the dried product layer. In the *product model* P_{sat} was no longer equal to P_C, instead P_{sat} was calculated assuming the mass flow through the porous layer was in Knudsen regime as [8,41]:

$$P_{sat} = P_C + \frac{\dot{m}\, R_P}{\frac{\pi}{4} {d_{VI}}^2} \tag{18}$$

where $\frac{\pi}{4} {d_{VI}}^2$ is the inner cross-section area of the vial. The Knudsen regime in the dried product layer was confirmed by estimating the mean free path at the sublimation front l_{fp} = 0.3 mm considering a product temperature equal to the maximal allowable value (T_{sat} = -32 °C, P_{sat} = 31 Pa) and an upper bound for the pore diameter taken from the literature (0.2 mm [42]). Two R_P values were taken from the literature [35] for a dried product layer thickness (l_d) of 0.1 and 5 mm as reported in Table 1. For l_d = 0.1 mm, the *product model* represents a stage of primary drying when 0.9 % of the product was dried in 500-µL vials or 0.6% of the product was dried in 1000-µL vials (% of dried product = [$l_d \times \frac{\pi}{4} {d_{VI}}^2 / V_p$] × 100%; Table 1). Moreover, for l_d = 5 mm, the *product model* represents a stage when 47% of the product was dried in 500-µL vials or 31% of the product was dried in 1000-µL vials (% of dried product = [$l_d \times \frac{\pi}{4} {d_{VI}}^2 / V_p$] × 100%; Table 1). The mass flux was related to the total heat flux at the sublimation front ($\dot{Q}$) (for the total vial, twice the value for the half-vial) via the following Equation:

$$\dot{m} = \frac{\dot{Q}}{\Delta H_{sub}} \tag{19}$$

6. COMSOL implementation

COMSOL Multiphysics 5.3a (COMSOL, Inc, Burlington, USA) is a simulation software used to solve partial differential equations. Heat transfer was simulated using the "Heat Transfer with Surface-to-Surface Radiation" module, and equations were solved using the geometric multigrid solver. This section details how COMSOL was used to simulate the heat transfer during ice sublimation in high-throughput vials inside well plates.

6.1. Imposed temperatures

The sublimation front was considered a flat ice-vapour interface at the top of the frozen layer contained in each vial. Moreover, the freeze dryer chamber was supposed saturated with water vapour [7,21,24,39]. Three surface temperatures were imposed in our system (Figure 3): (i) T_{sat}, calculated using Equation (17); (ii) T_{shelf}, which was considered as the average between the inlet and the outlet temperature of the heat-transfer fluid circulating inside the shelves; (iii) the wall temperature (T_{wall}), which was measured during the experiments (Section 4.2).

6.2. Definition of the heat transfer areas between adjacent surfaces

Minimal gaps between adjacent solid bodies observed in real objects were simplified in our models' geometry, so adjacent solids shared the same surface where heat transfer coefficients were applied. The well plate bottom in the geometry was flat and shared its surface with the bottom shelf below. Heat transfer from the bottom shelf to the well plate bottom (Figure 3c, orange dot 1) occurred through their shared area, where the K_{WP}^{cc}, K_{WP}^{gc}, and K_{WP}^{rad} were applied (in parallel, $K_{WP}^{cc} + K_{WP}^{gc} + K_{WP}^{rad}$). The well diameter was considered equal to the external vial diameter, so the well sides shared surfaces with the vial sides; moreover, the vial bottoms were deemed to be flat and sharing surface with the well bottoms. Heat transfer from the wells to the vials (Figure 3c, orange dots 2 and 2') occurred through their shared areas, where K_{HV}^{cc}, K_{HV}^{gc}, and K_{HV}^{rad} were applied as illustrated in Appendix (in parallel, $K_{HV}^{cc} + K_{HV}^{gc} + K_{HV}^{rad}$ or $K_{HV}^{gc} + K_{HV}^{rad}$).

6.3. Calculation of the heat flows

Calculations were performed with the Heat Transfer Surface-to-Surface Radiation physics interface of COMSOL by the finite-element method using a relative tolerance of 10^{-5} as a convergence criterion. The

Surface-to-Surface Radiation feature was used to calculate the view factors between surfaces by the hemi-cube method, taking into account the shadowing effect as previously done by Scutellà et al. [21]. For the *product model*, the consideration of a dried product layer implied an iterative calculation; for a given R_P, T_{sat} depends on P_{sat} hence on $\dot{Q}$ (Equations (17) to (19)). This iteration was performed using the LiveLink interface connecting MATLAB R2017a (The MathWorks, Inc, Natick, Massachusetts, USA) and COMSOL. The following iteration path was followed to solve the heat and mass transfer equations:

a) solving the 3D heat transfer model with an initial guess of T_{sat} values in each vial (using COMSOL), obtaining first-iterated $\dot{Q}$ values at the sublimation front for each vial;
b) calculating the new T_{sat} values using Equations (17) to (19) (using MATLAB), based on the first-iterated $\dot{Q}$ values;
c) solving the 3D heat transfer model with the new T_{sat} values (using COMSOL), obtaining the second-iterated $\dot{Q}$ values at the sublimation front for each vial;
d) comparing first-iterated and second-iterated $\dot{Q}$ values (using MATLAB);
e) repeating steps b) to d) until the difference between iterated $\dot{Q}$ values was smaller than 0.1%.

6.4. Parameter estimation

Five model parameters, relevant to heat transfer between adjacent solid surfaces, had to be estimated based on measured heat flows in selected conditions: K_{WP}^{cc}, K_{HV}^{cc}, α_{WP}, α_{HV}, and l_{WP}. Parameters were estimated using the experimental heat flows received by 500-µL vials at shelf temperature -15 °C and chamber pressures 4, 12, and 65 Pa. The estimation was performed by calculating the heat flows using the 3D model in COMSOL and tuning the parameters using a code containing the *nlinfit* function of the Statistics and Machine Learning Toolbox provided by MATLAB to match measured heat flows in a least-square sense. The LiveLink interface connected COMSOL and MATLAB. The final values of the parameters are presented in Table 2.

6.5. Sensitivity analysis

Investigating how variations in the parameters impact the model results is critical to identify sensitive parameters that require special effort for determination or control, in contrast to those parameters for which rough estimations are sufficient for practical purposes. The Morris' method [43] was used to classify the twenty model parameters listed in Table 3 according to their impact on $\dot{Q}$ received by the

central vials calculated using the *product model*. The range of each parameter was discretised in six uniformly distributed levels. Ten combinations of the twenty parameters and two operating conditions – hereinafter referred to as "domain samples" – were considered in this work. Domain samples were selected using the Latin hyper-cube sampling method, ensuring each parameter's level is selected once. The relative impact of the jth parameter in the ith domain sample (dimensionless sensitivity, $E_j^{(i)}$) was calculated as:

$$E_j{}^{(i)} = \frac{\dot{Q}\left(x_1{}^{(i)}, \dots, x_j{}^{(i)} + \Delta_j, \dots, x_{22}{}^{(i)}\right) - \dot{Q}\left(x_1{}^{(i)}, \dots, x_{22}{}^{(i)}\right)}{\Delta_j} \times \frac{\Gamma_j}{\dot{Q}\left(x_1{}^{(i)}, \dots, x_{22}{}^{(i)}\right)} \quad (20)$$

where $x_j{}^{(i)}$ is the value of the jth parameter in the ith domain sample, Γ_j is the range of the jth input, and Δ_j is the increment of the jth input. Input ranges and increments are given in Table 3, and Δ_j was considered as 10% of the range.

The limits of the value ranges (Table 3) were established for each input according to different criteria: (i) for the emissivity values, limits were the extreme values taken from the literature or measured using an emissometer EM-2 by Themacs Ingénierie (Champs sur Marne, France); (ii) for the geometric dimensions of the vials, limits were taken from extreme values measured by Precis&Mans (Le Mans, Pays de la Loire, France) using 96 vials of each size (500-µL and 1000-µL) and one well plate for the work presented in Buceta et al. [5]; (iii) for the geometric dimensions of the shelves and chamber wall, and for the surface temperature of the chamber wall, limits were taken from extreme values measured in this work; (iv) for the estimated parameters, the range was the 95% confidence interval; and (v) for the dried product resistance to the mass transfer, limits were the extreme values taken from the literature for a dried product layer thickness of 5 mm. Values of the parameters that depend on the dried product layer (i.e. ε_{dry}, λ_{dry}) were not found in the literature on freeze-drying. Therefore, the range of ε_{dry} went from 0 to 1 (minimal to maximal physically possible emissivity values). Moreover, the lower limit of the λ_{dry} range was 0 $W.m^{-1}.K^{-1}$, and the upper limit was considered as ten times the value initially considered.

Table 3 – Ranges of the model inputs values considered for the sensitivity analysis.

Input	Range	Units
Physical constants		
ε_{dry}	0 – 1	Dimensionless
ε_{shelf}	0.17* – 0.42*	Dimensionless
ε_{vial}	0.78[6] – 0.94[27]	Dimensionless
ε_{wall}	0.13* – 0.42*	Dimensionless
ε_{wp}	0.82[27] – 1.00	Dimensionless
λ_{dry}	0 – 0.43	$W.m^{-1}.K^{-1}$
Geometric dimensions		
d_C	$(9.6 – 12.0)\times10^{-2}$	m
d_E	$(1.10 – 1.4)\times10^{-1}$	m
d_S	$(5.0 – 6.6)\times10^{-2}$	m
d_{VI}	$(7.14 – 7.25)\times10^{-3}$	m
l_{HV}^B	$(4.4 – 9.0)\times10^{-5}$	m
l_{HV}^S	$(4.2 – 4.8)\times10^{-4}$	m
V_i	349 – 436	µL
	523 – 654	
V_p	392 – 479	µL
	587 – 717	
Estimated parameters		
K_{HV}^{cc}	12.1 – 28.1	$W.m^{-2}.K^{-1}$
K_{WP}^{cc}	1.6 – 8.6	$W.m^{-2}.K^{-1}$
l_{WP}	$(2.46 – 5.94)\times10^{-4}$	m
α_{HV}	0.287 – 0.373	Dimensionless
α_{WP}	0.597 – 1.303	Dimensionless
Other model parameters		
R_P	$(1[44] – 5[41])\times10^5$	$Pa.s.m^2.kg^{-1}$
T_{wall}	0 – 15	°C
Operating Conditions		
P_C	4 – 15	Pa
T_{shelf}	-40 – 0	°C

** Measured using an emissometer EM-2 by Themacs Ingénierie (Champs sur Marne, France).*

7. Results and discussion

7.1. Mesh convergence

The accuracy of the models' numerical solution depends on the resolution considered to discretise the system of equations within the geometry (meshing). Therefore, a convergence study was performed considering two meshes suggested by COMSOL (Table 4). The “coarse” meshes (for 500-µL and 1000-µL vials), with approximately 47% fewer elements and degrees of freedom than “normal” meshes, calculated heat flows that differed from “normal” meshes in less than 0.2% and were obtained in approximately 72% less time (average calculation time for all operating conditions). Given the experimental variability of the data (the average coefficient of variation was 11%), “coarse” meshes were considered robust enough for the study of both vial sizes (500-µL and 1000-µL vials) and were used throughout this work.

Table 4 – Convergence test.

Mesh	Number of degrees of freedom	Number of elements	Average calculation time for all operating conditions (min)	Maximum absolute difference in heat flow, relative to the “Normal” mesh (%)
500-µL vials				
Normal	212000	91000	29	NA
Coarse	107000	43000	7	0.2
1000-µL vials				
Normal	245000	106000	20	NA
Coarse	137000	56000	6	0.2

NA: not applicable.

7.2. Parameter estimation and model validation against experimental heat flows

Heat flows received by 500-µL vials under three operating conditions (Figure 4b, the nine striped bars) were used for model parameter estimation. The rest of the experimental data (Figure 4b and 4c, the twenty-seven white bars) were used for model validation.

Table 2 reports the values of the five parameters estimated (i.e. K_{WP}^{cc}, K_{HV}^{cc}, α_{WP}, α_{HV}, l_{WP}), which are related to the heat transfer between adjacent surfaces. Parameters' values were compared to those of previous work [5] where the same five parameters were estimated using a 0D model in steady-state considering the following simplifying hypothesis: (H1) all the heat flow received by the well plate came from the shelf below (bottom shelf, Figure 2), and (H2) all the heat flow received by central vials arrived from the well plate. To compare parameters' values of different works, the heat transfer areas considered for the heat transfer between adjacent surfaces should be the same. Therefore, the 95% confidence intervals of K_{HV}^{cc} and α_{HV} of 500-µL vials in "B-type well plates" (as referred in [5]) were multiplied by the heat transfer area of that work (outer cross-section area of the vial) and divided by the heat transfer areas of our work; the final values are reported in Table 2. The 95% confidence intervals of K_{WP}^{cc}, α_{WP}, and l_{WP} estimated in the previous and present work overlapped, suggesting that H1 was accurate enough to determine the coefficients involved in the heat transfer between the bottom shelf and the well plate. However, the confidence intervals of K_{HV}^{cc} did not overlap, suggesting that H2 was not valid and perhaps a considerable part of the heat received by the vials came from other hot surfaces in the chamber (e.g. top shelf).

The validation of the 3D model consisted of comparing the calculated heat flows received by the vials to the heat flows obtained through gravimetric analysis during ice sublimation experiments. The values of the heat flows were grouped according to the vial position inside de well plate (Figure 4a): (i) central vials (CV), (ii) inner edge vials (IEV), and (iii) outer edge vials (OEV). Figure 4b and 4c show the calculated heat flow rates (blue, grey and red bars) plotted next to the experimental values (white bars). The values of the heat flow received by the six central vials in each model geometry were averaged since the coefficient of variation was less than 2% among central vials. Differences between calculated and experimental heat flow rates used for parameter estimation were on average 2.2% of the experimental values, and 3.6% in the case of validation conditions; in all cases, differences were smaller than the experimental coefficient of variation (approximately 11%).

The agreement between the predicted and experimental heat flows was statistically tested by calculating the coefficient of determination (R^2). Figure 5 shows the predicted versus observed heat flows for all vial positions inside de well plate (i.e. CV, IEV, OEV). Data was close to the 1:1 line, and R^2 values were over 0.98, both results put forward the simulations' goodness. Thus, the model generalisation ability was considered adequate, and heat transfer simulations in new operating conditions (i.e. shelf temperature and chamber pressure) within the considered experimental range were thought reliable.

Additionally, the calculated temperature at the vial bottom was compared with the temperature values measured using the Tempris thermal probes, obtaining a good agreement (< 0.8 °C difference).

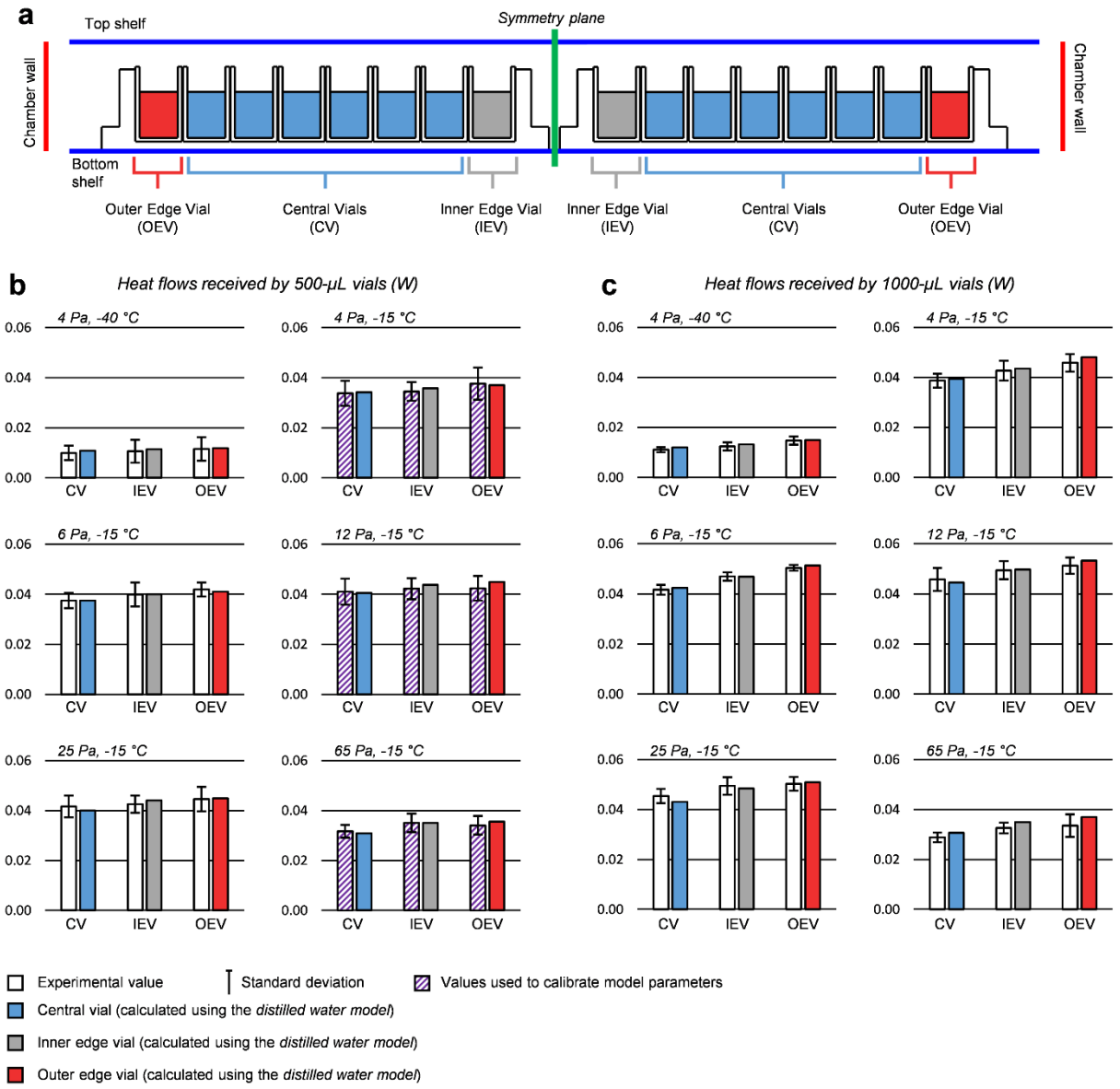

Figure 4 – (a) Vial positions in the well plate on the shelf (not in scale): central vials (CV, average flow of the six central vials in the geometry) in blue, inner edge vials (IEV) in grey, and outer edge vials (OEV) in red. (b) Comparison of experimental and simulated heat flows received by 500-µL vials. (c) Comparison of experimental and simulated heat flows received by 1000-µL vials. Several combinations of shelf temperatures (-40 °C and -15 °C) and chamber pressures (4, 6, 12, 25, and 65 Pa) were tested. Error bars in experimental data represent standard deviations.

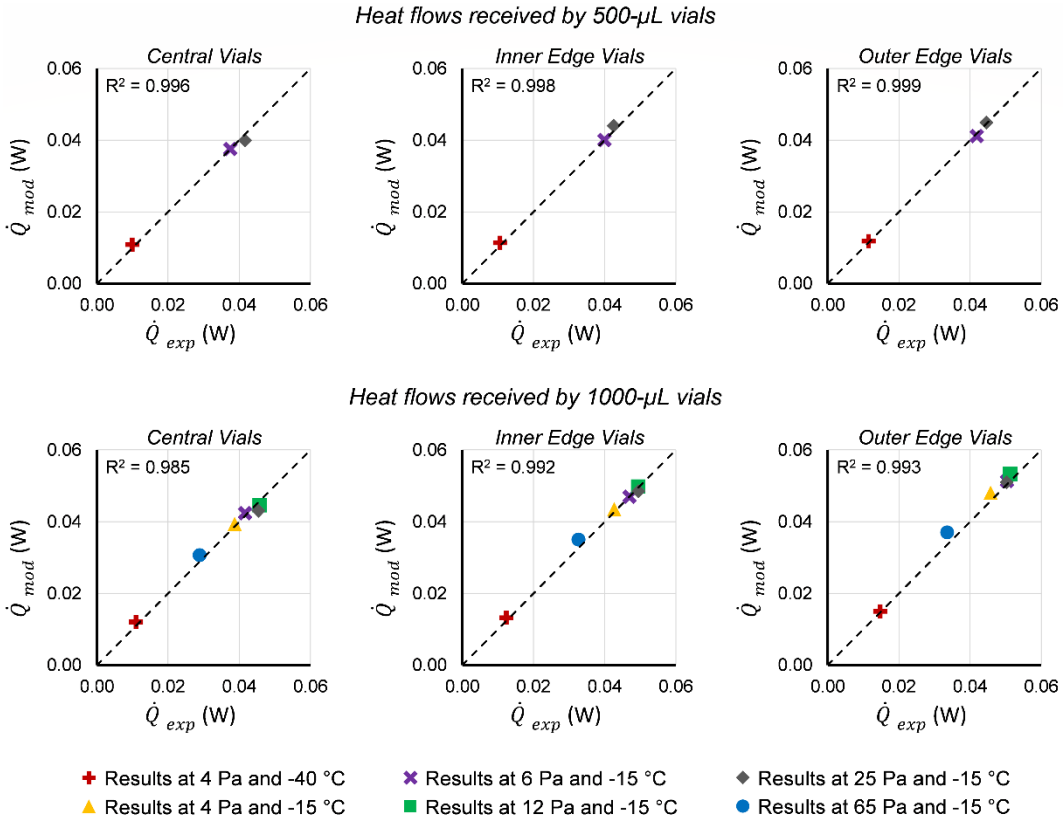

Figure 5 – $\dot{Q}_{exp}$ vs $\dot{Q}_{mod}$. The 1:1 dotted line represents perfect agreement between predicted and observed values. The values of the coefficient of determination (R^2) are reported in each graph.

7.3. Heat flow variations between different vial positions in the distilled water model

The impact of the vial position on the heat flow received by the vials during primary drying, commonly known as the “edge effect”, has been previously studied by several authors using serum vials filled with water (e.g. [7,15,21,25]). Scutellà et al. [21] observed that heat flows received by serum vials (filled with water) located at the periphery of the shelf increased by 47% compared to the heat flows received by serum vials in the centre of the arrangement (at shelf temperature 0 °C and chamber pressure 4 Pa); furthermore, Rambhatla and Pikal [15] (Figure 3 therein) reported an increase of 40% (at shelf temperature -25 °C and chamber pressure 13 Pa). In the case of high-throughput vials, a similar effect of the vial position in the well plate may be initially speculated; however, there is no published research or work to this date investigating this hypothesis.

Figure 6 shows the relative increase in the heat flow reaching high-throughput vials in the edge of the well plate ($\dot{Q}_E$) compared to those in the centre ($\dot{Q}_C$), expressed as the ratio of the heat flow rates ($\dot{Q}_E/\dot{Q}_C$). Two edge vials configurations were investigated: (i) edge vials facing the chamber wall (Outer Edge Vials, results in red in Figure 6), and (ii) edge vials facing another well plate (Inner Edge Vials, results in grey in Figure 6). Moreover, two vial sizes were considered: (i) 500-µL vials (striped bars) and (ii) 1000-µL vials (filled bars). Simulations were run at a chamber pressure of 4, 6 and 12 Pa and shelf temperatures of -40 °C and -15 °C. Considering outer edge vials, 500-µL vials exhibited a heat flow rate approximately 11% (= [$\dot{Q}_E$ / $\dot{Q}_C$ – 1] × 100%) greater than central vials, while reaching up to 25% (= [$\dot{Q}_E$ / $\dot{Q}_C$ – 1] × 100%) for 1000-µL vials (worst case 4 Pa and -40 °C). However, when considering inner edge vials, the heat flow increase compared to central vials was lower than 11% (= [$\dot{Q}_E$ / $\dot{Q}_C$ – 1] × 100%), regardless of the vial’s size.

Placing a 1000-µL vial in an outer edge position instead of a central position had the most critical impact on the heat flow received (19% to 25%; = [$\dot{Q}_E$ / $\dot{Q}_C$ – 1] × 100%). This impact seemed to increase with lower shelf temperatures and lower chamber pressures, as previously noted between serum vial positions on the shelf [15,21]. However, for 500-µL vials and 1000-µL inner edge vials, the impact of the high-throughput vial position in the well plate could be considered negligible compared to that of serum vials (over four times lower [15,21]).

The use of 500-µL vials would be recommended to avoid heat transfer variations between vial positions in the well plate. However, screening tests may frequently require sampled volumes over 500 µL; hence,

1000-µL vials may be the only alternative. The results for 1000-µL vials should be considered as a worst-case situation.

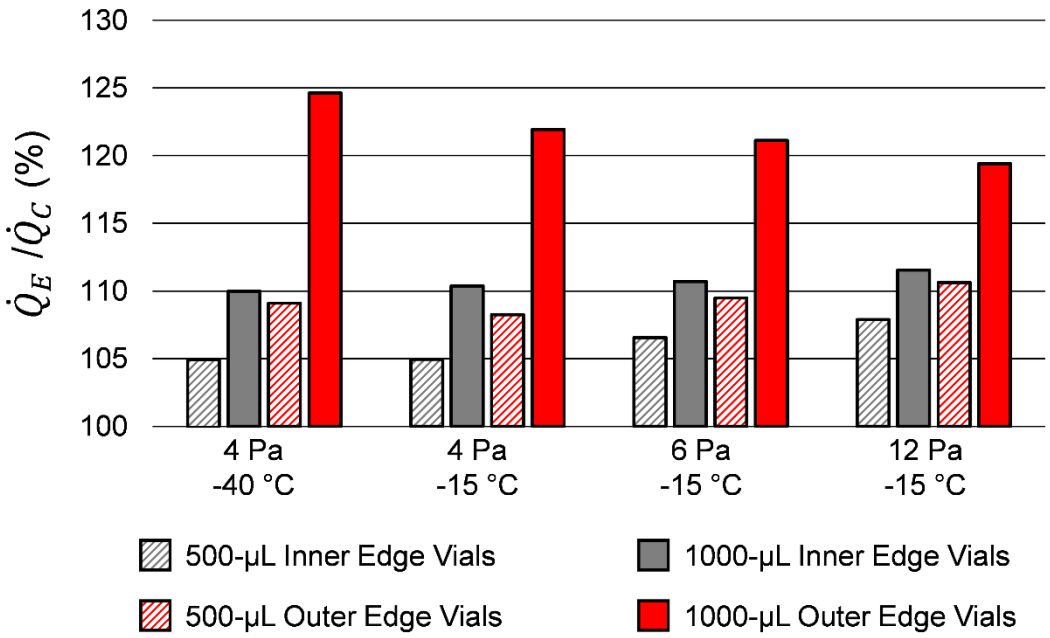

Figure 6 – Ratio (%) of $\dot{Q}_E$ to $\dot{Q}_C$ (= [$\dot{Q}_E$ / $\dot{Q}_C$] × 100%). Results were obtained using the distilled water model at different shelf temperatures (-40 and -15 °C) and chamber pressures (4, 6 and 12 Pa). Vial positions refer to those shown in Figure 2.

7.4. Temperature profile and heat flux distribution in the distilled water model

The temperature profiles and the heat fluxes in the drying chamber were simulated using 3D modelling. As an example, Figure 7 shows the results obtained at shelf temperature -15 °C and chamber pressure 4 Pa using the *distilled water model*. The temperature profiles are represented as colour maps, and heat fluxes are represented as arrows whose lengths indicate their module on a logarithmic scale to accentuate the visualisation of the smaller fluxes. Two vial sizes were considered: 500-µL vials (Figure 7a) and 1000-µL vials (Figure 7b). For each vial size, the geometry presented an outer edge vial, an inner edge vial, and six central vials. Comparing 500-µL and 1000-µL vials, 1000-µL edge vials received extra heat fluxes through the vial area protruding from the well plate, which explains why placing a vial in an edge position was more critical for the heat flow received in the case of 1000-µL vials than 500-µL vials. These extra heat fluxes came mostly from the top shelf and chamber wall in the case of 1000-µL outer edge vials, and from the top shelf in the case of 1000-µL inner edge vials.

The difference between the maximal and minimal temperature in the well plate was less than 0.16 °C. Hence, the well plate temperature could be considered homogenous compared to the rest of the system's temperature variations, e.g. 4.4 °C between the vials and the well plate and 24.7 °C between the well plate and the shelf at chamber pressure 4 Pa and shelf temperature -15 °C. Such low variation within the well plate temperature was due to the aluminium's high conductivity [5,27]. The temperature difference within the ice/frozen layer was less than 2.0 °C due to the relatively high thermal conductivity of the ice compared to the vapour in the vial headspace and the chamber (> 80 times greater). The highest temperature in the ice/frozen layer occurred at the bottom of the content and the lowest temperature (T_{sat}) was observed at the ice sublimation front, as noted in previous modelling studies [16,21]. Remarkably, the heat flux in the ice/frozen layer was essentially one-directional, coming from the bottom to the top (following the temperature gradient direction) despite lateral heat transfer to the vial sides from the metallic pillars and well plate walls.

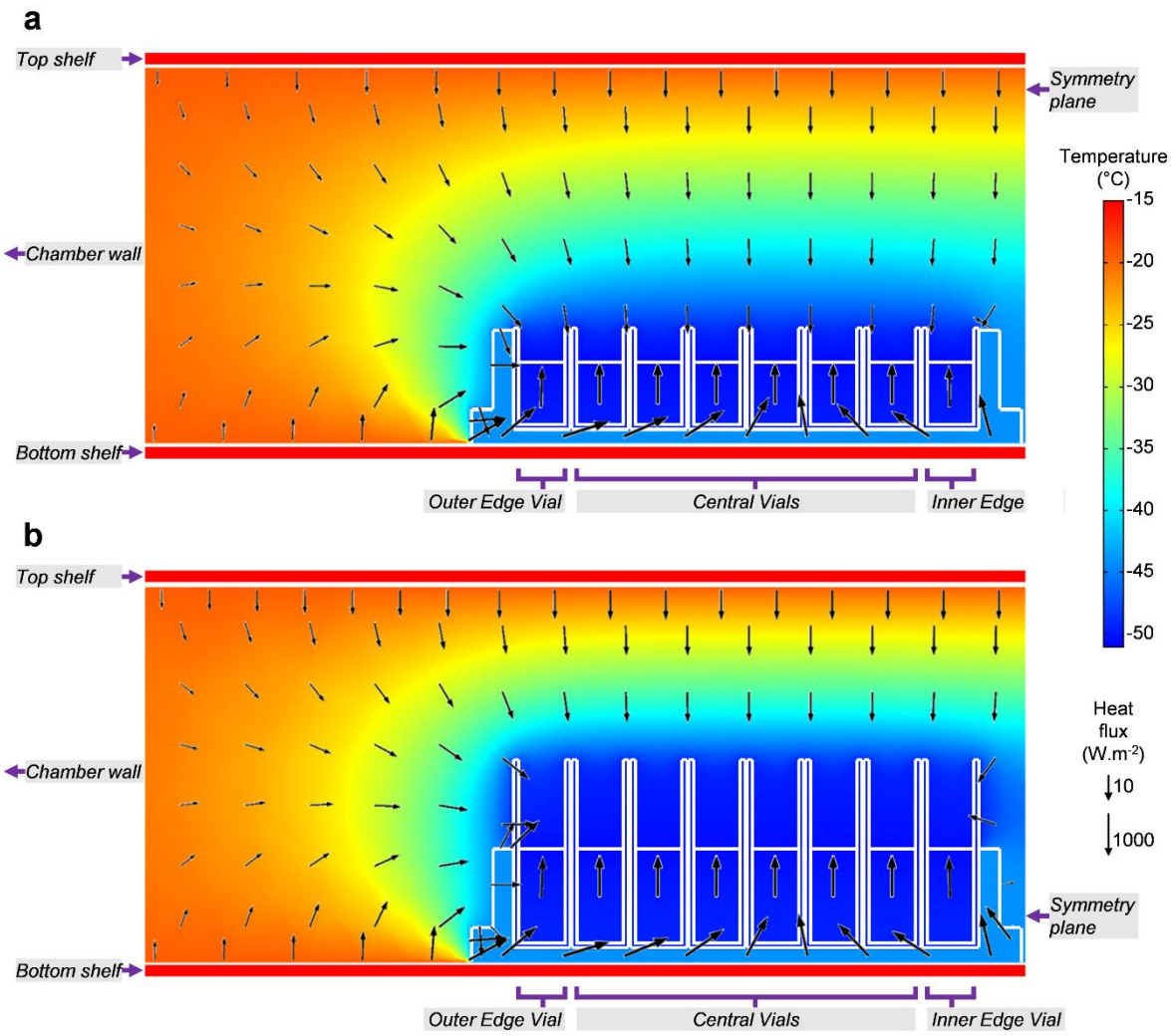

Figure 7 – Temperature profiles and heat fluxes obtained with the distilled water model for (a) 500-µL vials and (b) 1000-µL vials. Temperatures are represented as colour maps. Heat fluxes through the loose gas, vials and frozen product layers are represented as arrows whose lengths indicate their module on a logarithmic scale. Calculations were performed at a shelf temperature of -15 °C and a chamber pressure of 4 Pa.

7.5. Relative importance of individual heat transfer mechanisms in the distilled water model

According to the *distilled water model*, 1000-µL vials in outer edge positions received higher heat flows than in central positions (Figure 6), while this tendency was less pronounced when using 500-µL vials. To identify which heat transfer mechanisms were responsible for these observations, Figure 8a presents the heat flow contributions of each mechanism received by 500-µL and 1000-µL vials (respectively) calculated using the *distilled water model* at chamber pressure 4 Pa and shelf temperature -15 °C. Most of the heat flow received by the vials came from the well (over 50% of the total heat flow; e.g. 0.028 W out of the total 0.048 W received by the outer edge 1000-µL vial in Figure 8a), primarily by contact conduction (over 39% of the total heat flow; e.g. 0.019 W out of the total 0.048 W received by the outer edge 1000-µL vial in Figure 8a).

Regarding vial sizes, the heat contribution of radiation from distant surfaces in central vials increased from 500-µL vials to 1000-µL vials (e.g. from 0.0022 W for 500-µL vials to 0.0064 W for 1000-µL vials in Figure 8a), and so did the conduction through the gas within the chamber (e.g. from 0.0044 W for 500-µL vials to 0.0065 W for 1000-µL vials in Figure 8a). Comparing 1000-µL edge vials to central vials (Figure 8a), the greater heat flow received by the inner edge vial (up to 11%, = $[\dot{Q}_E/\dot{Q}_C] \times 100\%$) was due to conduction through the gas within the chamber, and the even greater heat flow received by the outer edge vial (up to 25%, = $[\dot{Q}_E/\dot{Q}_C - 1] \times 100\%$) also had a contribution of radiation from distant surfaces. These results put forward that the impact of the vial position was due to the heat flow contributions received through the vial surface protruding from the well plate. 500-µL vials protrude less than 0.1 cm from the well-plate, while 1000-µL vials protrude around 1 cm (half of the total vial height). Thus, the greater height of 1000-µL vials, compared to 500µ-L vials, exposed them more to radiation and gas conduction from the chamber. At the same time, the well plate considerably protected the 500-µL vials from such heat flow contributions, consequently limiting the edge effect.

In the case of serum vials, most authors attribute the edge effect to the heat transfer by radiation from the chamber surfaces [7,15,18–20,24,25], while Scutellà et al. [21] concluded through 3D mathematical modelling that the main “extra” heat contribution from the chamber wall was transferred by gas conduction to the serum vials. In the case of high-throughput vials, radiation and gas conduction from distant surfaces had similar contributions in the *distilled water model***.**

The *distilled water model* could be considered as a representation of the beginning of primary drying when there is no dried product layer (hence no dried product resistance, R_P = 0). As drying continues,

a dried product layer forms and progresses from the top of the frozen layer and increases P_{sat} and T_{sat} at the sublimation front, therefore affecting the heat received by the product. The following Section 7.6 will study how a dried product layer's presence could affect the heat transfer by using the *product model*. Moreover, we could interpret the variation in the heat flow received by different vial positions “in time” during primary drying by comparing the *distilled water model* results (representing the beginning of primary drying) and the *product model* results (representing an advanced moment during primary drying).

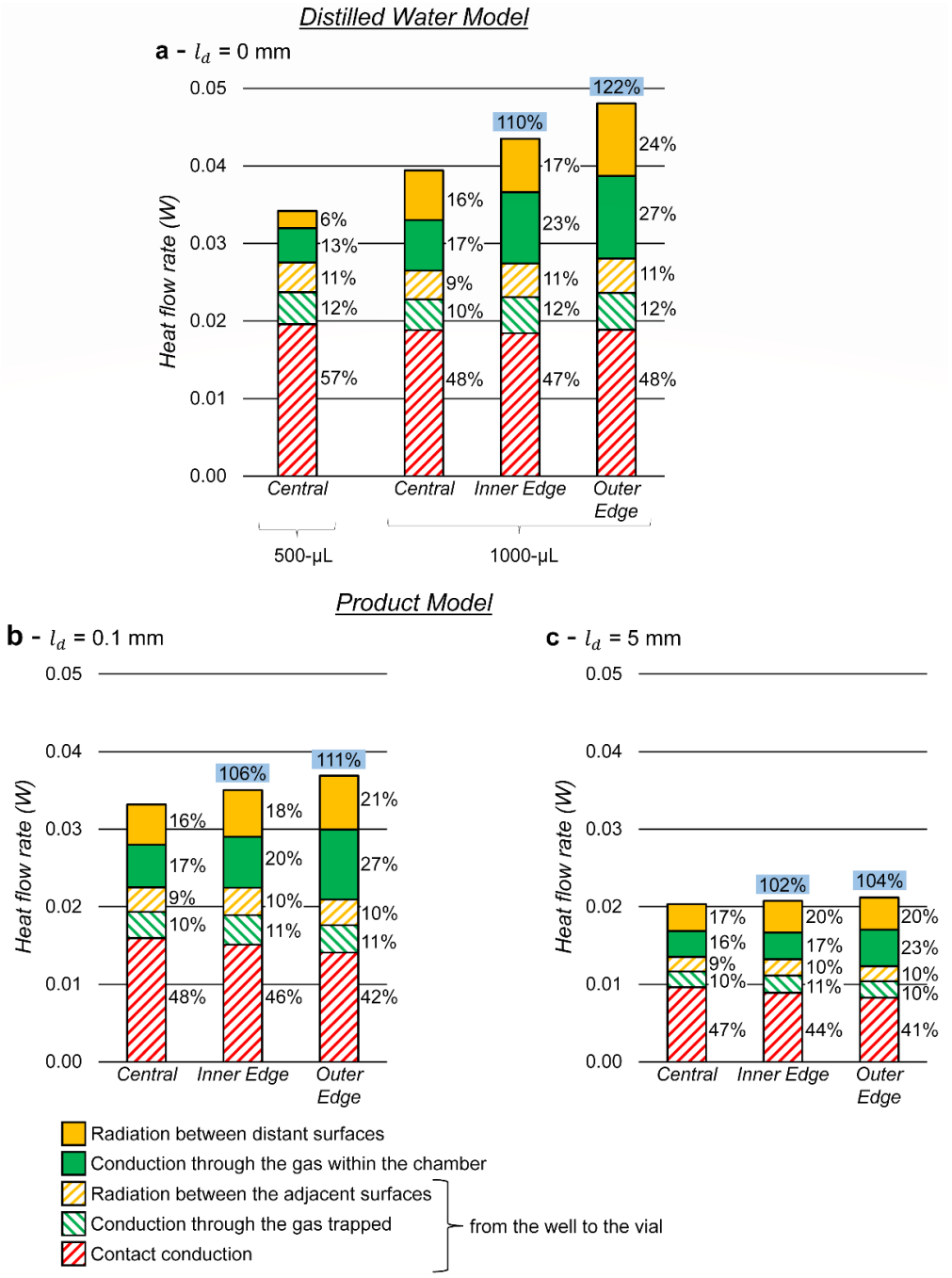

Figure 8 – Heat flow rates and their relative contributions to the total heat flow received by the vials using (a) the distilled water model for 500-µL vials and 1000-µL vials; and using the product model for 1000-µL vials considering a dried layer thickness (l_d) of (b) 0.1 mm and (c) 5 mm. Blue squares report the ratio (%) of $\dot{Q}_E$ to $\dot{Q}_C$ (= [$\dot{Q}_E$ / $\dot{Q}_C$] × 100%). Relative contribution (%) of each mechanism with respect to $\dot{Q}_C$ (= [heat flow contribution / $\dot{Q}_C$] × 100%) are reported next to the corresponding bar. Calculations were performed at a shelf temperature of -15 °C and a chamber pressure of 4 Pa. Central, Inner Edge, and Outer Edge refer to vial positions detailed in Figure 2.

7.6. Heat flow variations between different vial positions in the product model

By considering the resistance to the mass transfer imposed by a dried product layer, the *product model* gives an insight into how the heat flow variations among vial positions observed in the *distilled water model* will evolve as ice sublimation progresses during primary drying. Figure 8b and 8c present the heat flows received by 1000-µL vials calculated using the *product model* at chamber pressure 4 Pa and shelf temperature -15 °C. Two R_P values corresponding to different l_d were considered in this work, one representing an early stage of primary drying (Figure 8b, l_d = 0.1 mm, R_P = 0.119×10^5 Pa.s.m^2.kg^{-1}), and another representing a more advanced stage (Figure 8c, l_d = 5 mm, R_P = 1.248×10^5 Pa.s.m^2.kg^{-1}). As expected, heat flows received by the vials decreased when R_P increased. For example, the heat flow received by central vials decreased by 50% (= [$\dot{Q}_C$ in the *product model* / $\dot{Q}_C$ in the *distilled water model*] × 100%) compared to the *product model* at l_d = 5 mm (Figure 8a vs Figure 8c). This occurred because R_P increased P_{sat} and hence T_{sat}, which reduced the temperature difference between the sublimation front of all the vials and the hot surfaces (i.e. shelves and chamber wall), and ultimately the total heat flow to the vials.

Variations in the heat flows received by vials in different positions were smaller in the *product model* than in the *distilled water model* and decreased when R_P increased. As it was previously mentioned in Section 7.3, outer edge vials presented heat flows up to 25% (= [$\dot{Q}_E$ / $\dot{Q}_C$ – 1] × 100%) greater than central vials in the distilled water model (Figure 6, 1000-µL vials). In the *product model*, however, such increase in the heat flow from central to outer edge vials was 11% (= [$\dot{Q}_E$ / $\dot{Q}_C$ – 1] × 100%) at l_d = 0.1 mm (blue square in Figure 8b) and only 4% (= [$\dot{Q}_E$ / $\dot{Q}_C$ – 1] × 100%) at l_d = 5 mm (blue square in Figure 8c). Thus, the edge effect is expected to diminish throughout primary drying as R_P increases, which is a beneficial practical outcome.

The heat flow from the top shelf and the chamber door (red, yellow, and green plain bars in Figure 8) increased from central to edge vials in the *distilled water* and *product models*, being the main cause of the heat flow variations between vial positions. In the *distilled water model*, T_{sat} only depends on the chamber pressure so all vials were essentially at the same temperature. In the *product model*, however, T_{sat} increased with the total heat flow received (as described above and in Section 6.3), so the edge vials were slightly warmer (< 1 °C) than the central vials, as further discussed in the following Section 0.

7.7. Temperature profile in the product model

Figure 9 shows the temperature profiles of an outer edge vial and a central vial considering different dry layer thicknesses (l_d values). Product temperature profiles in the outer edge and central vials are similar at the beginning of primary drying (Figure 9a, l_d = 0 mm) when the temperature at the sublimation front (-51.5°C) is determined by the chamber pressure alone. In contrast, the introduction of a dried product layer entailed a higher product temperature in outer edge vials (-44.3°C at the sublimation front) compared to central vials (-45.0°C) (Figure 9b, l_d = 0.1 mm) due to the coupling between heat and mass transfer: a higher heat flow near the edge induced a higher mass flow through the porous layer (Equation (19)), which resulted in a higher pressure at the sublimation front (Equation (18)) and hence in a higher temperature at this surface (Equation (17)). As primary drying continued (Figure 9c, l_d = 5 mm) and R_P increased, the overall vial temperature increased, e.g. by about 10 °C from figure Figure 9b to Figure 9c. Thus, heat flows to the vials decreased (Figure 8b vs Figure 8c) because they depend on the temperature difference between the hot surfaces (mainly shelves) and the vials. This difference between shelf and vial temperatures was larger for the “colder” central vials than for the “warmer” edge vials. As a result, in the *product model*, the larger heat flow received from the shelves by the “colder” central vials partly compensated the extra heat flow received from the walls by the edge vials, explaining the reduction of the edge effect as l_d increased. Ultimately, the temperature difference between edge and central vials diminished (0.4 °C in Figure 9b vs 0.2 °C in Figure 9c), which is a favourable consequence for product homogeneity.

Figure 9 also indicates that the temperature differences within the dried product layer were always less than 1.1 °C. Most lumped-variable (0D) models do not consider heat conduction through the dry layer and calculate the product temperature at the sublimation front (lowest temperature in the dried product layer). Consequently, an additional safety margin should be considered for process design based on T_{sat} to avoid collapse in any part of the dried product layer.

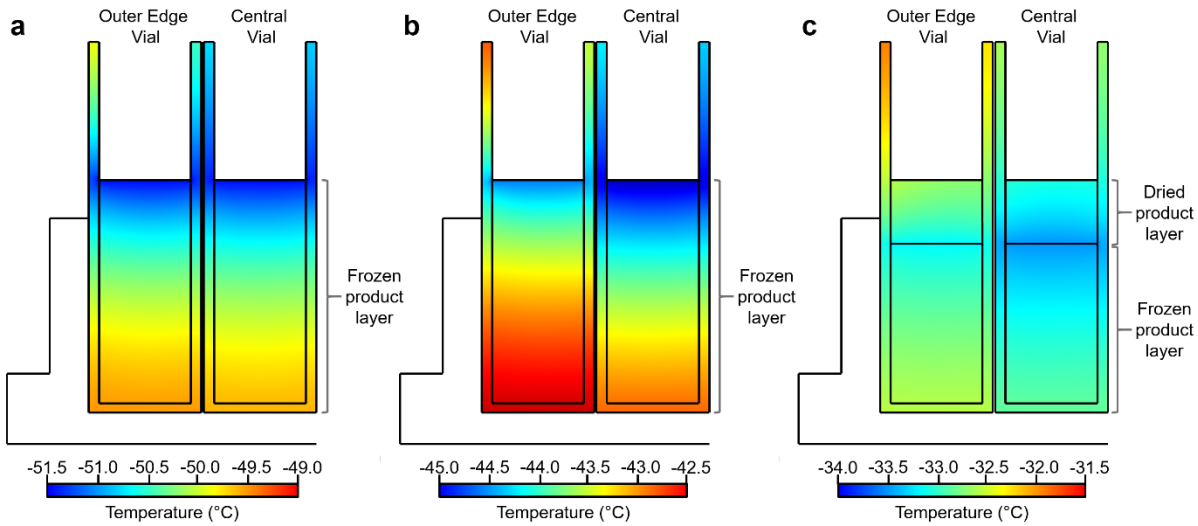

Figure 9 – Temperature profiles for 1000-µL outer edge and central vials for a filling height of 16 mm, obtained with (a) the distilled water model (l_d= 0 mm), (b) the product model considering l_d= 0.1 mm, and (c) the product model considering l_d= 5 mm. Temperatures are represented as colour maps; note the same temperature span (2.5°C) in each case. Calculations were performed at a shelf temperature of -15 °C and a chamber pressure of 4 Pa.

7.8. Sensitivity analysis

A sensitivity analysis was performed to identify the model parameters (inputs) that should be more precisely determined when calculating heat flows received by the vials ($\dot{Q}$) using the *product model*. The relative impacts of the variation of each parameter on the calculated heat flow received by all vial positions (i.e. central, inner edge, outer edge) and vial sizes (i.e. 500-µL and 1000-µL) were similar.

Figure 9 – Temperature profiles for 1000-µL outer edge and central vials for a filling height of 16 mm, obtained with (a) the distilled water model (l_d= 0 mm), (b) the product model considering l_d= 0.1 mm, and (c) the product model considering l_d= 5 mm. Temperatures are represented as colour maps; note the same temperature span (2.5°C) in each case. Calculations were performed at a shelf temperature of -15 °C and a chamber pressure of 4 Pa.

Figure 10 presents the average values and standard deviations of E_j for central 1000-µL vials. Positive E_j values refer to an increase in the heat flow when increasing the parameter value, while negative values denote a decrease. The most sensitive parameters were: (i) α_{WP}, (ii) K_{WP}^{cc}, and (iii) R_P. α_{WP} and K_{WP}^{cc} are related to the well plate bottom surface, their high sensitivity indicates the key role of the heat transfer between the bottom shelf and the well plate bottom (limiting resistance) on the total heat transfer to the sublimation front [5]. The importance of K_{WP}^{cc} is in agreement with previous research using serum vials, which highlighted the impact of the contact conduction between the shelf and the serum vial bottom [6,7,14,45]. However, while α_{WP} was found as a sensitive parameter, to the best of our knowledge, well plate-to-well plate variation has not been studied in the literature. Manufacturing glass serum vials appears to entail lower vial-to-vial variations in the surface finish compared to the well-plate-to-well-plate variations caused by the aluminium turning technique observed in this study. The high impact of R_P highlighted the importance of the mass transfer during primary drying. The negative value of the R_P sensitivity (Figure 10) indicates that an increase of R_P tends to reduce the heat transfer to the vial. Similar results were obtained when performing the sensitivity analysis with l_d values in a lower range (0 to 0.1 mm; data not shown).

On another note, many heat and mass transfer models for the primary drying do not take into account heat transfer parameters depending on the dried product layer (i.e. ε_{dry}, λ_{dry}) (e.g. [6,39,46]). The sensitivity of ε_{dry} and λ_{dry} were over 20 times lower than that of the most sensitive parameter (α_{WP}),

confirming that much experimental effort does not need to be put in their determination and rough estimations are sufficient.

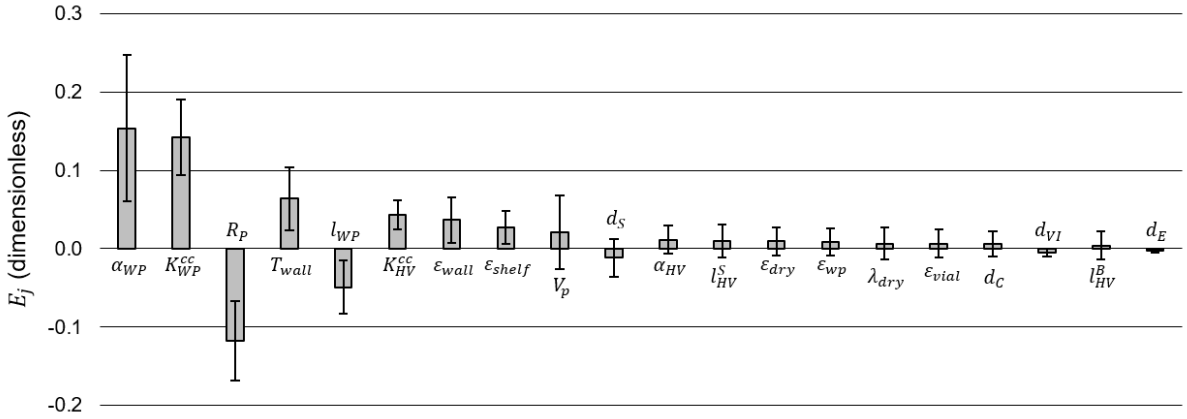

Figure 10 – E_j values of the parameters reported in Table 3, calculated using Equation (20). Grey bars represent the average values for the domain samples, and error bars represent the standard deviations within the "domain samples".

8. Conclusions

This work studied heat transfer mechanisms and the edge effect in a high-throughput and well plate system (i.e. heat flow increase in vials facing the chamber wall) using 3D modelling. Two 3D steady-state models were developed and compared: one representing the beginning of primary drying with only frozen water, and another one representing intermediate stages of primary drying (for a sucrose aqueous solution) by including the formation and progress of a dried product layer.

The edge effect was only significant in vials protruding from the well plate (1000-µL vials) and at the very beginning of primary drying. The edge effect is thus expected to diminish throughout primary drying as the dried product layer thickness increases. Our work suggested that heat transfer variations due to the vial position in the well plate are caused by the heat flow contributions from the chamber wall and top shelf by radiation and conduction through the gas within the chamber. Interestingly, compared to freeze-drying in serum vials, the presence of a metallic well plate significantly reduce the impact of the vial position (over 50%, = 100% × [$\dot{Q}_E$ / $\dot{Q}_C$] in high-throughput vials / [$\dot{Q}_E$ / $\dot{Q}_C$] in serum vials) in all studied situations by improving the heat transfer from the bottom shelf and redistributing a portion of the extra heat flow from the chamber wall to the high-throughput vials (i.e. central and edge).

Based on the models presented in this work, further model development could help to understand the impact of the well plate position on the shelf.

9. Conflicts of interest

Erwan Bourlés and Bernadette Scutellà are employees of the GSK group of companies. Juan Buceta participated in a post-graduate PhD programme at GSK. Stéphanie Passot, Fernanda Fonseca and Ioan Cristian Tréléa report no financial conflicts of interest.

10. Funding

This work was funded by GlaxoSmithKline Biologicals S.A., under a Cooperative Research and Development Agreement with the Institut National de la Recherche pour l'Agriculture, l'Alimentation et l'Environnement (INRAE) via the intermediary of the Unité Mixte de Recherche (UMR), Paris Saclay Food and Bioproducts Engineering (SayFood) at the INRAE, Versailles-Grignon Research Centre.

11. Author's contributions

Juan Buceta, Stéphanie Passot, Bernadette Scutellà, Erwan Bourlés, Fernanda Fonseca and Ioan Cristian Trelea were involved in the conception and design of the study. Juan Buceta, Bernadette Scutellà and Erwan Bourlés acquired the data. Juan Buceta, Stéphanie Passot, Bernadette Scutellà, Erwan Bourlés, Fernanda Fonseca and Ioan Cristian Trelea analysed and interpreted the results. All authors were involved in drafting the manuscript or critically revising it for relevant intellectual content. All authors had full access to the data and approved the manuscript before it was submitted by the corresponding author.

12. **Appendix**

The geometry between the adjacent surfaces of the wells and the vials was modified to simplify the COMSOL model. Figure 11a is a 3D reconstruction of a real well plate with pillars between the wells. Furthermore, Figure 11b presents the 3D geometry of a simplified well plate without pillars, assuming that wells are not connected and have a diameter equal to the external vial diameter.

Figure 12a shows the cut of the well plate initially aimed at being represented in the model geometry. Figure 12b presents the modified well plate geometry obtained by considering the well diameter equal to the external vial diameter, so the well sides share surfaces with the vial sides. Figure 12c details the physical meaning of each portion of the surface shared between the wells and the vials. The shared surface include: (i) a bottom portion where the well bottom faces the vial bottom; (ii) a lateral portion where the physical contact pillar faces the vial, (iii) a lateral portion where the other pillar (in the case of a central well) or the well plate wall (in the case of an edge well) faces the vial side, and (iv) a lateral portion where the vial faces an adjacent vial. The lateral surfaces shared between the wells and the vials were divided into eight equal parts where different coefficients were applied according to Figure 12c. K_{HV}^{gc} and K_{HV}^{rad} were applied in surface portions corresponding to wells facing vials (continuous orange surfaces and orange striped surfaces in Figure 12c). K_{HV}^{cc} was applied in surface portions corresponding to a well bottom and a physical contact pillar facing a vial (continuous orange surfaces in Figure 12c). The heat transfer through the lateral surfaces between vials (green surfaces in Figure 12c) was considered negligible compared to the transfer from the well plate, which corresponds to assuming a symmetry condition between vials.

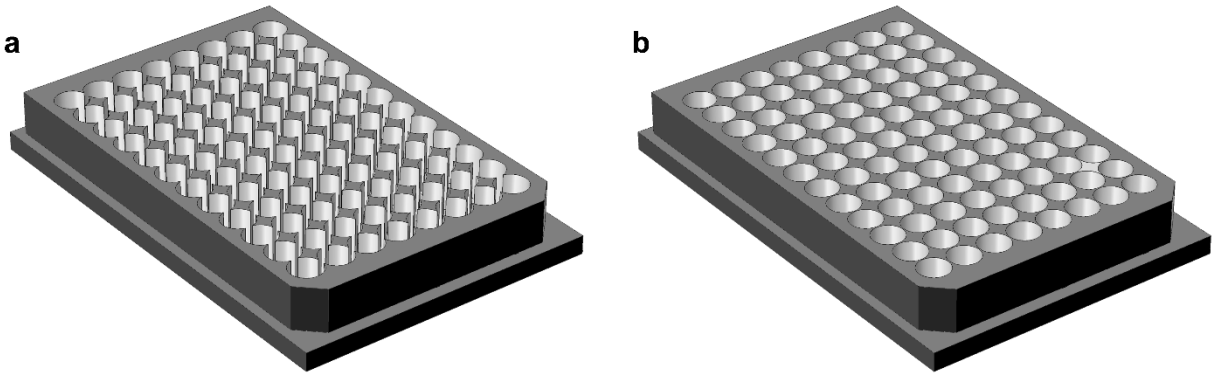

Figure 11 – 3D reconstruction of a well plate. (a) Geometry of a "real" well plate with pillars. (b) Geometry of a simplified well plate without pillars, assuming the well diameter equal to the external vial diameter.

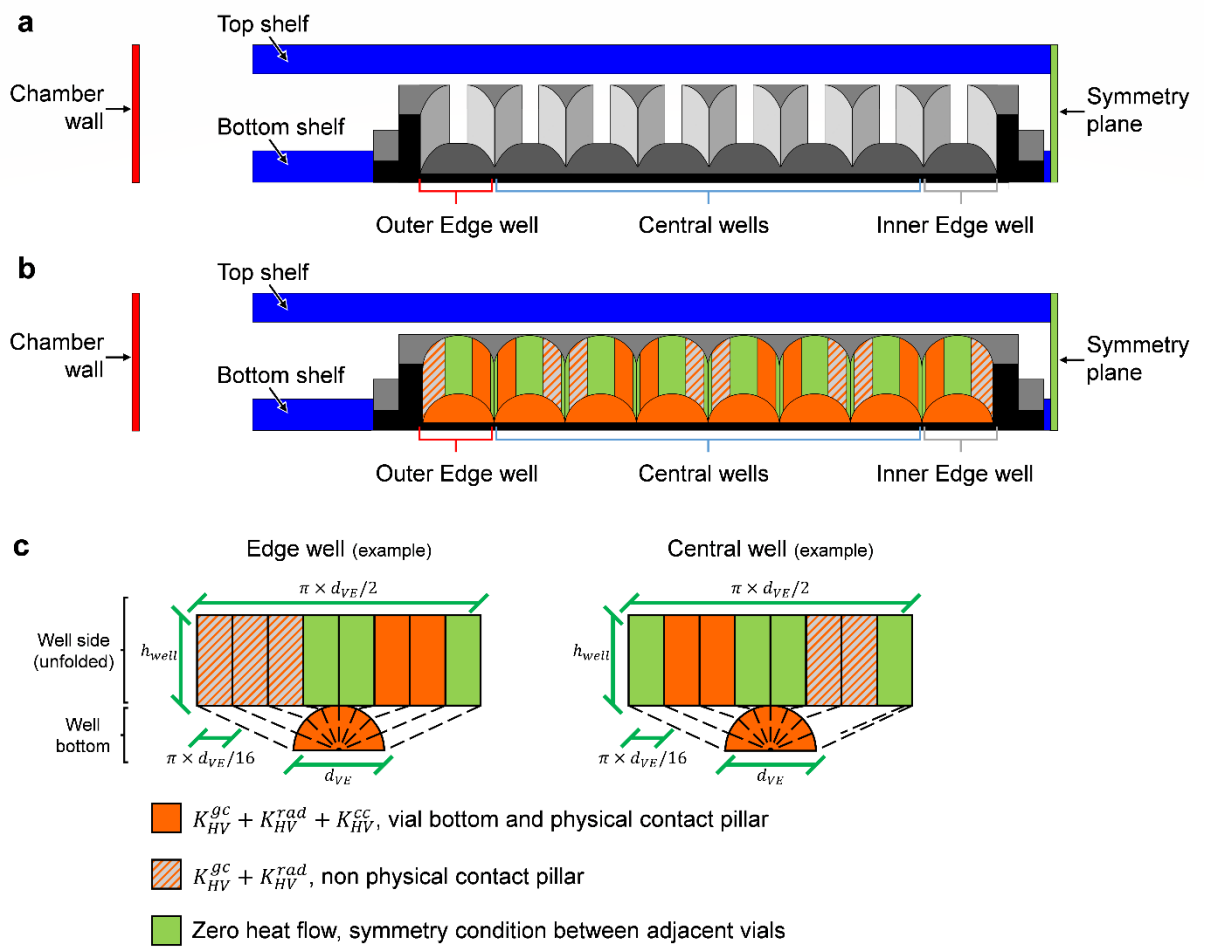

Figure 12 – Schematic representation (not in scale) of the heat transfer area and coefficients between the wells and the vials (not in scale). (a) View from top of the well plate cut considered in the geometry (vials are not shown). (b) View from top of the well plate cut considered in the geometry when assuming the wells and the vials share the same surface equal to the external vial diameter (vials are not shown). (c) Surface shared by the wells and the vials where heat transfer coefficients were applied. Geometric dimensions refer to Table 1. K_{HV} *are detailed according to the heat transfer mechanism involved:* K^{cc} *by contact conduction,* K^{gc} *is by conduction through the gas trapped between the surfaces,* K^{rad} *by radiation.*

13. References

[1] E. Bourlés, G. de Lannoy, B. Scutellà, F. Fonseca, I.C. Tréléa, S. Passot, Scale-Up of Freeze-Drying Cycles, the Use of Process Analytical Technology (PAT), and Statistical Analysis: New Technologies and Approaches, in: Methods Pharmacol. Toxicol., 2019: pp. 215–240. https://doi.org/10.1007/978-1-4939-8928-7_10.

[2] S. Passot, F. Fonseca, S. Cenard, I.C. Tréléa, Developing smart control strategies of freeze-drying of lactic acid bacteria, in: 5th Int. Conf. Lyophilization Free. Dry., Bologne, Italy, 2012. https://hal.archives-ouvertes.fr/hal-01628100 (accessed November 16, 2020).

[3] M.J. Pikal, K. Dellerman, M.L. Roy, Formulation and stability of freeze-dried proteins: effects of moisture and oxygen on the stability of freeze-dried formulations of human growth hormone, Dev. Biol. Stand. 74 (1992) 21–37; discussion 37-38.

[4] S. von Graberg, Freeze Drying from Small Containers: Heat and Mass Transfer and Implications on Process Design, ResearchGate. (2011). https://www.researchgate.net/publication/296063173_Freeze_Drying_from_Small_Containers_Heat_and_Mass_Transfer_and_Implications_on_Process_Design (accessed February 7, 2019).

[5] J.P. Buceta, I.C. Tréléa, B. Scutellà, E. Bourlés, F. Fonseca, S. Passot, Heat transfer during freeze-drying using a high-throughput vial system in view of process scale-up to serum vials, J Pharm Sci. (2020). https://doi.org/10.1016/j.xphs.2020.11.029.

[6] B. Scutellà, S. Passot, E. Bourlés, F. Fonseca, I.C. Tréléa, How Vial Geometry Variability Influences Heat Transfer and Product Temperature During Freeze-Drying, J Pharm Sci. 106 (2017) 770–778. https://doi.org/10.1016/j.xphs.2016.11.007.

[7] R. Pisano, A.A. Baressi, D. Fissore, Heat transfer in freeze-drying apparatus, in: Dev. Heat Transf., M.dos Santos Bernardes, Rijeka, Croatia, 2011: pp. 91–114.

[8] D. Fissore, R. Pisano, A.A. Barresi, Advanced approach to build the design space for the primary drying of a pharmaceutical freeze-drying process, J Pharm Sci. 100 (2011) 4922–4933. https://doi.org/10.1002/jps.22668.

[9] S.M. Patel, S.L. Nail, M.J. Pikal, R. Geidobler, G. Winter, A. Hawe, J. Davagnino, S. Rambhatla Gupta, Lyophilized Drug Product Cake Appearance: What Is Acceptable?, J Pharm Sci. 106 (2017) 1706–1721. https://doi.org/10.1016/j.xphs.2017.03.014.

[10] B. Vanbillemont, N. Nicolaï, L. Leys, T. De Beer, Model-Based Optimisation and Control Strategy for the Primary Drying Phase of a Lyophilisation Process, Pharmaceutics. 12 (2020) 181. https://doi.org/10.3390/pharmaceutics12020181.

[11] M.J. Pikal, S. Shah, The collapse temperature in freeze drying: Dependence on measurement methodology and rate of water removal from the glassy phase, Int. J. Pharm. 62 (1990) 165–186. https://doi.org/10.1016/0378-5173(90)90231-R.

[12] S. Nail, J. Searles, Elements of quality by design in development and scale-up of freeze parenterals, BioPharm Int. 21 (2008) 44–52.

[13] S.A. Velardi, A.A. Barresi, Development of simplified models for the freeze-drying process and investigation of the optimal operating conditions, Chem. Eng. Res. Des. 86 (2008) 9–22. https://doi.org/10.1016/j.cherd.2007.10.007.

[14] M. Brülls, A. Rasmuson, Heat transfer in vial lyophilization, Int. J. Pharm. 246 (2002) 1–16.

[15] S. Rambhatla, M.J. Pikal, Heat and mass transfer scale-up issues during freeze-drying, I: Atypical radiation and the edge vial effect, AAPS PharmSciTech. 4 (2003) 22–31. https://doi.org/10.1208/pt040214.

[16] P. Sheehan, A.I. Liapis, Modeling of the primary and secondary drying stages of the freeze drying of pharmaceutical products in vials: Numerical results obtained from the solution of a dynamic and spatially multi-dimensional lyophilization model for different operational policies, Biotechnol. Bioeng. 60 (1998) 712–728. https://doi.org/10.1002/(SICI)1097-0290(19981220)60:6<712::AID-BIT8>3.0.CO;2-4.

[17] S.M. Patel, T. Doen, M.J. Pikal, Determination of End Point of Primary Drying in Freeze-Drying Process Control, AAPS PharmSciTech. 11 (2010) 73–84. https://doi.org/10.1208/s12249-009-9362-7.
[18] M.J. Pikal, M.L. Roy, S. Shah, Mass and Heat Transfer in Vial Freeze-Drying of Pharmaceuticals: Role of the Vial, J Pharm Sci. 73 (1984) 1224–1237. https://doi.org/10.1002/jps.2600730910.
[19] S. Schneid, H. Gieseler, Evaluation of a New Wireless Temperature Remote Interrogation System (TEMPRIS) to Measure Product Temperature During Freeze Drying, AAPS PharmSciTech. 9 (2008) 729–739. https://doi.org/10.1208/s12249-008-9099-8.
[20] L. Wegiel, S. Ferris, S. Nail, Experimental Aspects of Measuring the Vial Heat Transfer Coefficient in Pharmaceutical Freeze-Drying, AAPS PharmSciTech. 19 (2018). https://doi.org/10.1208/s12249-018-0998-z.
[21] B. Scutellà, A. Plana-Fattori, S. Passot, E. Bourlés, F. Fonseca, D. Flick, I.C. Tréléa, 3D mathematical modelling to understand atypical heat transfer observed in vial freeze-drying, Appl Therm Eng. 126 (2017) 226–236.
[22] A. Giordano, A.A. Barresi, D. Fissore, On the Use of Mathematical Models to Build the Design Space for the Primary Drying Phase of a Pharmaceutical Lyophilization Process, J Pharm Sci. 100 (2011) 311–324. https://doi.org/10.1002/jps.22264.
[23] V.R. Koganti, E.Y. Shalaev, M.R. Berry, T. Osterberg, M. Youssef, D.N. Hiebert, F.A. Kanka, M. Nolan, R. Barrett, G. Scalzo, G. Fitzpatrick, N. Fitzgibbon, S. Luthra, L. Zhang, Investigation of Design Space for Freeze-Drying: Use of Modeling for Primary Drying Segment of a Freeze-Drying Cycle, AAPS PharmSciTech. 12 (2011) 854–861. https://doi.org/10.1208/s12249-011-9645-7.
[24] M.J. Pikal, Heat and mass transfer in low pressure gases: applications to freeze-drying, in: Transp. Process. Pharm. Syst., Marcel Dekker, Inc., New York, 2000: pp. 611–686.
[25] M.J. Pikal, R. Bogner, V. Mudhivarthi, P. Sharma, P. Sane, Freeze-Drying Process Development and Scale-Up: Scale-Up of Edge Vial Versus Center Vial Heat Transfer Coefficients, Kv, J. Pharm. Sci. 105 (2016) 3333–3343. https://doi.org/10.1016/j.xphs.2016.07.027.
[26] J.S. D'Arrigo, Screening of membrane surface charges by divalent cations: an atomic representation, Am J Physiol Cell Physiol. 235 (1978) C109–C117. https://doi.org/10.1152/ajpcell.1978.235.3.C109.
[27] R.H. Perry, D.O. Green, Perry's chemical engineers' handbook, 8th ed., McGraw-Hill, 2008.
[28] D.M. Murphy, T. Koop, Review of the vapour pressures of ice and supercooled water for atmospheric applications, Q J R Meteorol Soc. 131 (2005) 1539–1565. https://doi.org/10.1256/qj.04.94.
[29] H. Emteborg, R. Zeleny, J. Charoud-Got, G. Martos, J. Lüddeke, H. Schellin, K. Teipel, Infrared Thermography for Monitoring of Freeze-Drying Processes: Instrumental Developments and Preliminary Results, J Pharm Sci. 103 (2014) 2088–2097. https://doi.org/10.1002/jps.24017.
[30] D.R. Heldman, C.I. Moraru, Encyclopedia of Agricultural, Food, and Biological Engineering, CRC Press, 2010.
[31] W.M. Haynes, ed., CRC Handbook of Chemistry and Physics, 95th Edition, 95 edition, CRC Press, Boca Raton; London; New York, 2014.
[32] M. S. van Dusen, International Critical Tables of Numerical Data, Physics, Chemistry and Technology, NAP, Washington, DC, 1929.
[33] D.S. Smith, A. Alzina, J. Bourret, B. Nait-Ali, F. Pennec, N. Tessier-Doyen, K. Otsu, H. Matsubara, P. Elser, U.T. Gonzenbach, Thermal conductivity of porous materials, J. Mater. Res. 28 (2013) 2260–2272. https://doi.org/10.1557/jmr.2013.179.
[34] T. Renaud, P. Briery, J. Andrieu, M. Laurent, Thermal properties of model foods in the frozen state, J. Food Eng. (1992). https://agris.fao.org/agris-search/search.do?recordID=US201301741795 (accessed June 9, 2021).
[35] A.K. Konstantinidis, W. Kuu, L. Otten, S.L. Nail, R.R. Sever, Controlled nucleation in freeze-drying: Effects on pore size in the dried product layer, mass transfer resistance, and primary drying rate, J Pharm Sci. 100 (2011) 3453–3470. https://doi.org/10.1002/jps.22561.

[36] W.J. Mascarenhas, H.U. Akay, M.J. Pikal, A computational model for finite element analysis of the freeze-drying process, Comput Method Appl M. 148 (1997) 105–124. https://doi.org/10.1016/S0045-7825(96)00078-3.
[37] W.L. Heitz, J.W. Westwater, Critical Rayleigh Numbers for Natural Convection of Water Confined in Square Cells With L/D From 0.5 to 8, J. Heat Transf. 93 (1971) 188–195. https://doi.org/10.1115/1.3449783.
[38] D. Hoffman, B. Singh, J. Thomas III, Handbook of Vacuum Science and Technology, 1st ed., Academic Press, Elsevier, 1997. https://www.elsevier.com/books/handbook-of-vacuum-science-and-technology/hoffman/978-0-12-352065-4 (accessed March 3, 2020).
[39] M.J. Pikal, Use of laboratory data in freeze drying process design: heat and mass transfer coefficients and the computer simulation of freeze drying, J Parenter Sci Technol. 39 (1985) 115–139.
[40] R. van Eck, M. Kelp, J. van Schijnde, Surface to surface radiation benchmarks, in: Comsol Conf., Munich, Germany, 2016.
[41] B. Scutellà, I.C. Trelea, E. Bourlès, F. Fonseca, S. Passot, Determination of the dried product resistance variability and its influence on the product temperature in pharmaceutical freeze-drying, Eur J Pharm Biopharm. 128 (2018) 379–388. https://doi.org/10.1016/j.ejpb.2018.05.004.
[42] I. Oddone, P.-J. Van Bockstal, T. De Beer, R. Pisano, Impact of vacuum-induced surface freezing on inter- and intra-vial heterogeneity, Eur J Pharm Biopharm. 103 (2016) 167–178.
[43] M.D. Morris, Factorial Sampling Plans for Preliminary Computational Experiments, Technometrics. 33 (1991) 161–174.
[44] D. Fissore, R. Pisano, Computer-Aided Framework for the Design of Freeze-Drying Cycles: Optimization of the Operating Conditions of the Primary Drying Stage, Processes. 3 (2015) 406–421. https://doi.org/10.3390/pr3020406.
[45] W.Y. Kuu, S.L. Nail, Rapid freeze-drying cycle optimization using computer programs developed based on heat and mass transfer models and facilitated by tunable diode laser absorption spectroscopy (TDLAS), J. Pharm. Sci. 98 (2009) 3469–3482. https://doi.org/10.1002/jps.21813.
[46] S.T.F.C. Mortier, P.-J. Van Bockstal, J. Corver, I. Nopens, K.V. Gernaey, T. De Beer, Uncertainty analysis as essential step in the establishment of the dynamic Design Space of primary drying during freeze-drying, Eur J Pharm Biopharm. 103 (2016) 71–83. https://doi.org/10.1016/j.ejpb.2016.03.015.